3. Numerical Modelling[1]

3.1 Introduction

Low-level wind maxima have been frequently observed in the boundary layer of tropical cyclones. In the introduction, a physical mechanism for producing such a jet was described in which strong inwards advection of angular momentum leads to supergradient flow. A key point was that some process must maintain the inflow against the outward acceleration due to gradient adjustment. In Chapter 2, a linear analytical model of the boundary layer of a moving tropical cyclone was presented, and used to show that vertical diffusion could maintain inflow in the presence of a weakly supergradient jet in the upper boundary layer. A significant short-coming was that the jet was too weak. However calculation of the relevant forcing terms, and the development of a supplementary model with a crude representation of the vertical motion showed that this was probably due to the neglect of vertical advection there. In a moving storm, it was found that the jet was stronger (more supergradient) on the left side of a northern hemisphere cyclone. Surface-wind factors were also calculated, and found to increase towards the centre of the storm. There was also a broad left-right asymmetry in surface-wind factor, with larger values on the weaker, left (right) side of the storm in the Northern (Southern) Hemisphere. The two components that made up the motion-induced asymmetry were shown to be due to frictionally stalled inertia waves with azimuthal wave-number one.

---

[1]Material similar to this chapter was published as Kepert and Wang (2001). The lowest model level there was 22.5 m, while here it is the wind-measurement standard of 10 m. Thus the model "near-surface" winds, and related quantities, are slightly lighter here, than in the original publication.

A high-resolution, full primitive equation dry hydrostatic numerical model of the tropical cyclone boundary layer, forced by an imposed pressure gradient, will be presented in this chapter. It relaxes the constraint of linearity from Chapter 2, includes the full advection terms, and will be seen to produce a markedly stronger jet, more consistent with the observations. The contribution of the various terms in the momentum budget equations will be quantified, and it is confirmed that the vertical advection of inflow is of major importance in jet dynamics. Its neglect was therefore the main reason that the linear model produced too weak a jet. An analysis of the flow in the boundary layer of an inertially neutral cyclone will be presented. This important case is beyond the scope of the linear model. Other improvements include a much more realistic representation of the turbulence, which is used to show that the jet is not a consequence of frictional decoupling due to near-surface stabilisation resulting from the cold near-surface conditions observed by Korolev et al. (1990), Black et al. (1993) and Cione et al. (2000).

It will be shown that the jet in a stationary storm is between 10% and 25% supergradient near the RMW, depending on the particular characteristics of the storm. The linear model height scale of $(2K/I)^{1/2}$, where K is the turbulent diffusivity and I the inertial stability, is shown to fit the numerical modelling results well. In the case of a moving Northern Hemisphere storm, the jet is shown to most supergradient – several times stronger than in a stationary storm – at the eyewall to the left and front of the storm, as well as extending into a significant area around to the left of the storm. It is, however, much less marked to the right, where the strongest winds are found. This asymmetry is in good agreement with that found earlier, and is dominated by the wave number 1 response forced by the asymmetric friction. The depth scales found in the numerical results are analysed and found to be in good agreement with those predicted

by the linear analysis.

The surface-wind factor will be shown to have a substantial spatial variability, similar to that found in the linear model. In particular, larger values are found near the eye, and there is an overall increase from right to left (left to right) of the storm in the Northern (Southern) Hemisphere, both consistent with the linear theory.

The model is described in the next section. It is applied to stationary storms in section 3.3, and moving storms in section 3.4. Particular attention will be paid to the nonlinear terms and the relationship of the results to those from the linear theory. The final section of this chapter contains further discussion and conclusions.

3.2 Model Formulation

As in chapter 2, the tropical cyclone boundary-layer is regarded as the frictional response to some known, steady-state cyclone in the free atmosphere, which is prescribed by an analytical profile. The influence that details of the boundary-layer structure may have on the cyclone as a whole are explicitly excluded from the analysis. While these clearly exist – for example, the pattern of boundary-layer convergence will affect the distribution of convection and hence heating – the scope here is rather to explore just one side of what is undoubtedly a two-way interaction. Also, there is no attempt to resolve the effects of convection on the boundary-layer, concentrating rather on larger scales. While studies (e.g. Powell 1990a, b, Barnes and Powell 1995) have shown significant modulation of boundary-layer structure in the vicinity of rain bands on scales comparable to the band width, the focus of this study is on building an understanding of the larger scale features of the tropical cyclone boundary-layer.

Accordingly, a shallow model domain is used, with the top boundary condition including a translating parametric pressure field intended to represent the remainder of the cyclone. A benefit of this approach is that it allows much higher vertical resolution in the boundary-layer than is customary in the numerical simulation of tropical cyclones, as there is no need to waste grid levels on resolving the entire storm. In most of the simulations presented here, the top boundary is set at 2.25 km. A further benefit is that the intensity, radial wind profile and movement of the storm, are easily and independently adjustable.

Consistent with the focus on the boundary-layer as a response to the "free atmosphere" flow, the representation of that by a parametric pressure field, and the neglect of convection, moisture is excluded from the model. Had it been included, its

sole role (apart from that of passive tracer) would be a tiny contribution to the height variation of pressure, through the hydrostatic equation.

Tropical cyclones are known to support a variety of instabilities that may result in the formation of smaller scale structures embedded in the flow. These transient features would complicate the analysis, without contributing to understanding of the larger-scale boundary-layer structure. Some are suppressed by the use of a prescribed fixed pressure field here, but it is necessary to carefully choose this so that the barotropic instability analysed by Schubert et al. (1999) is not supported. In the real atmosphere, it is expected that the cyclone-scale boundary-layer flow described here may be modulated by these smaller scale features.

3.2.1 Governing equations

The boundary-layer model is based on the three-dimensional nonlinear primitive equations of a dry, continuously stratified, hydrostatic atmosphere. The governing equations[2] are

[2]The numerical model is formulated in Cartesian coordinates, while the linear model of Chapter 2 and the analysis of results to come are in cylindrical coordinates. Although u and v are used for the velocity components in both coordinate systems and there is thereby a risk of confusion, the context will always make it clear which is intended.

$$\frac{du}{dt} = fv - \theta\frac{\partial \pi}{\partial x} + K_H\nabla^4 u + \frac{\partial}{\partial z}\left(K_v\frac{\partial u}{\partial z}\right)$$

$$\frac{dv}{dt} = -fu - \theta\frac{\partial \pi}{\partial y} + K_H\nabla^4 v + \frac{\partial}{\partial z}\left(K_v\frac{\partial v}{\partial z}\right)$$

$$\frac{d\theta}{dt} = K_H\nabla^4\theta + \frac{\partial}{\partial z}\left(K_h\frac{\partial \theta}{\partial z}\right) \qquad \textbf{(3.1)}$$

$$\frac{\partial \pi}{\partial z} = -\frac{g}{\theta}$$

$$\frac{\partial u}{\partial x} + \frac{\partial v}{\partial y} + \frac{\partial w}{\partial z} = 0$$

where

$$\frac{d}{dt} = \frac{\partial}{\partial t} + u\frac{\partial}{\partial x} + v\frac{\partial}{\partial y} + w\frac{\partial}{\partial z} \qquad \textbf{(3.2)}$$

and

$$\pi = C_p\left(\frac{p}{p_0}\right)^{R/C_p} \qquad \textbf{(3.3)}$$

is the Exner function with p_0 = 1000 hPa. In these equations, u, v and w are wind components in the x-, y- and z-directions respectively, θ is the potential temperature, f the Coriolis parameter (evaluated at 15°N), p the pressure, C_p the specific heat capacity of dry air at constant pressure, g the gravitational acceleration, K_H the horizontal diffusion coefficient, and K_v and K_h the turbulent vertical diffusivities for momentum and heat, respectively.

3.2.2 Physical parameterisations

The horizontal diffusion is calculated according to Smagorinsky et al. (1965)

with the modifications by Grell et al. (1994) to enhance the damping of short waves, and the diffusion coefficient given by

$$K_H = \frac{1}{2} k^2 \Delta^4 |D| \qquad \textbf{(3.4)}$$

where $k = 0.4$ is the von Kármán constant, Δ is the horizontal grid spacing and $|D|$ the total horizontal deformation. For the simulations presented here, this gives maximum values of $\Delta^2 K_H$ in the range $2 - 4 \times 10^3$ m^2 s^{-1} near the radius of maximum winds.

The vertical turbulent exchange coefficients are given by the turbulence closure scheme, which is the quasi-equilibrium E-*l* scheme of Galperin et al. (1987), also known as the level 2 1/4 scheme in the Mellor-Yamada hierarchy. A potential problem with the Mellor-Yamada schemes is that there are parts of the parameter space where some of the basic assumptions are violated, and the scheme can produce grossly unphysical results. This is generally avoided by the use of some "realisability conditions" to ensure reasonable behaviour when application of the scheme is not formally justified. The properties of the Mellor-Yamada level 2 ½ scheme were analysed in detail by Helfand and LaBraga (1988) and Gerrity et al. (1994), who showed that when the turbulent kinetic energy was substantially below its equilibrium value in statically unstable conditions, the scheme became unphysical and even included singularities. In particular, the turbulent kinetic energy production rates could be either negative or infinite in that part of the parameter space, when they should clearly be positive but finite. Here, the crucial assumption of Mellor and Yamada was that the turbulence is approximately isotropic. This is untrue in rapidly growing turbulence in an unstably stratified situation, where the large buoyant production term will be associated with a much larger variance of vertical velocity, than of horizontal.

A similar analysis of the level 2 1/4 scheme was carried out. It was found that although the details of the unphysical behaviour was different, the overall features, and severely deleterious effect on numerical modelling, were similar. Realisability conditions based on those proposed by Helfand and LaBraga (1988) and Gerrity et al. (1994) were imposed.

Surface fluxes are handled by Monin-Obukhov similarity theory with over-sea roughness lengths according to Charnock (1955) as modified by Smith (1988) for momentum, and Liu et al. (1979) as modified by Fairall et al. (1996) for heat and moisture. The Charnock coefficient is 0.011 as recommended by Fairall et al. (1996) throughout this chapter. The literature offers a range of values for this parameter up to at least 0.035 (Garratt 1992, Table 4.1). It is generally accepted as varying with water depth and fetch, and there are also several studies suggesting a sensitivity to wave age (e.g. Donelan et al. 1993, Maat et al. 1990, Toba et al. 1990). The value adopted is appropriate for long fetch, mature waves and deep water, and may therefore be on the low side for tropical cyclones. The effect of varying it will be discussed briefly in chapter 4. The sea surface temperature is held fixed and constant at 300 K.

3.2.3 Numerical Method

The governing equations are discretized and numerically integrated over an unstaggered grid in the horizontal and a staggered grid in the vertical. To reduce the size of the domain, a translating coordinate system is used in which the lower boundary together with the mesh of the model is shifted backward so that the parameterised tropical cyclone is stationary in the model domain. This results in the addition of a vector equal to the cyclone translation velocity to the horizontal advection flow. The horizontal mesh in the simulations presented consists of 201 by 201 grid points with a uniform grid

spacing of 5 km, unless stated otherwise.

There vertical grid is stretched in the vertical, with the midpoints of the 20 layers at z = 10, 23, 39, 60, 87, 121, 165, 222, 294, 386, 504, 655, 849, 1049, 1249, 1449, 1649, 1849, 2049 and 2249 m. Horizontal velocity, potential temperature, and Exner function are defined at these midpoints, with the vertical velocity w and turbulence variables (including the turbulent kinetic energy, mixing length, and vertical diffusivities) on the interfaces.

A two-time-level, explicit time-split scheme similar to that used in Wang (1998) is used for the model time integration. The procedure consists of an adjustment stage followed by an advection stage, and then the physical process stages. The same time step of 24 s is used for all stages to reduce the time-split errors. The time step is rather smaller than required by the Courant-Friedrichs-Lewy (CFL) criterion to reduce errors in the splitting of the nearly-balanced adjustment and centripetal (carried by the horizontal advection) terms.

Horizontal advection is calculated using the forward-in-time upstream scheme developed by Wang (1996). This has third-order accuracy for time-dependent and non-uniform flow, and possesses very weak dissipation, very small phase errors, and good shape-conserving properties. The order of calculating the u- and v- advection is alternated each time step to improve accuracy.

The adjustment stage is accomplished by the forward-backward scheme with the Coriolis force term treated implicitly in order to dampen inertial oscillations. The horizontal pressure gradient at the top of the model is known exactly from the applied

pressure field, and the small differences to this in the remainder of the model are calculated by integrating the horizontal gradient of the hydrostatic equation downwards from the upper boundary, using centred second-order differences for the horizontal temperature gradient. As the horizontal pressure gradient at any level is due almost entirely to the prescribed upper boundary condition, the use of a lower order of accuracy for the discretization of the horizontal temperature gradient is unimportant.

Vertical advection is calculated by a second-order, centred differencing scheme, with vertical motion diagnosed by integrating the continuity equation upwards from the surface. Thus mass is allowed to enter or exit the top of the model as required by the local net horizontal convergence.

Vertical diffusion is accomplished by a semi-implicit centred scheme with weight 1.5 on a future time step (Kalnay and Kanamitsu 1988), to avoid the nonlinear numerical instabilities often found in parameterisations of vertical turbulent transport. The horizontal diffusion is discretised via a centred second-order scheme for the space derivatives, and a forward time stepping scheme.

The model was run out for 24 hours, by which time all fields had attained an almost steady state. The use of a time split integration scheme greatly facilitated the calculation of budgets, which were done by saving the model state after each successive physical process was calculated. These were transformed from Cartesian into cylindrical coordinates and the tendency due to each physical process calculated from successive saves.

3.2.4 Initial and Boundary Conditions

The initial condition was that winds in gradient balance with the prescribed pressure field, except in the lowest level where they were reduced by 35%, primarily to ensure they remained within the validity range of the surface-layer scheme. The temperature field was stably stratified with a Brunt-Vaisala frequency of 10^{-3} s^{-1}.

The pressure field at the top of the model is prescribed using a slight modification of the analytical profile of Holland (1980), translating with the prescribed velocity. A uniform pressure gradient to represent the environmental boundary-layer flow was added. In the calculations presented here, this is set equal to the cyclone translation. The Holland (1980) profile has a number of advantages, as discussed in chapter 2. A minor deficiency is that it has a reversed radial vorticity gradient within the radius of maximum winds and therefore satisfies the necessary conditions for barotropic instability (Schubert et al., 1999). This is clearly an undesirable feature for the forcing of a numerical model such as this, as energy will be continually available to be fed into the unstable barotropic modes, but the concomitant horizontal mixing will not remove the source of the instability, as it would in the real atmosphere or a fuller model. Accordingly, the profile inside the RMW is modified to have a cubic dependence of V on r,

$$V(r) = c_1 r + c_2 r^2 + c_3 r^3, \qquad r < r_{\max} \tag{3.5}$$

where c_1, c_2, and c_3 are chosen to make V and its first two derivatives continuous at the RMW. A cubic dependence was chosen as this was similar to the stable profiles in Schubert et al. (1999) and was the simplest modification which had continuous radial derivatives of vorticity and inertial stability. The linear model results indicate the need for a continuously differentiable radial profile of vorticity, in that (2.25) shows that

discontinuities there will lead to discontinuities in *w*, which is undesirable as it could cause numerical problems or unphysical results[3]. The profile used is relatively broad at the RMW, while observed profiles are often quite sharp there. This may have a small effect on the relative jet strength very close to the RMW. However, a sharper profile cannot be easily tested in the present model because of the need to not support barotropic instability[4].

In the cases analysed here, the prescribed environmental flow is the same as the cyclone translation, so the gradient wind is the sum of the environment and vortex flows. This is easily shown by changing to a coordinate system moving with the vortex. The flow at the top of the model would not be expected to be exactly in gradient balance, even in the absence of discretisation and roundoff errors, since the dynamics there includes horizontal and vertical diffusion, and vertical advection. Moreover, the asymmetric component of the linear model of chapter 2 may still have an amplitude of 1 or 2 m s^{-1} at the model top, as the depth scale δ_{-1} of the dominant asymmetric component is similar to the model depth. It is important that the top boundary condition used should not interfere with similar structures in this model. To check, one integration was performed with double the domain depth, and the results found to be very similar

[3]In fact, an earlier attempt at modifying the flow within the eye used a quadratic rather than cubic, so that the vorticity and inertial stability were merely continuous. This resulted in a split eyewall updraft in the upper part of the model domain, with one local maximum inside, and another outside, the radius of maximum winds.

[4]Willoughby (2002) has very recently proposed a new parametric profile which is sharper at the RMW than Holland's, and can be formulated to be barotropically stable in the eye. It is used for some of the observational comparisons in Chapter 4, but became available too late for the analysis in this chapter.

to those obtained from the usual domain, including the representation of the asymmetric flow at these levels.

The remainder of the upper boundary condition is that vertical gradients of heat, velocity and turbulent kinetic energy are zero.

The lower boundary condition for mass is that $w = 0$. The lower boundary condition for turbulent kinetic energy is derived by assuming balance between dissipation and production terms in the turbulent energy equation, and by applying Monin-Obukhov similarity theory.

On the lateral boundaries, a radiation boundary conditions after Miller and Thorpe (1981) is used. A trial was also made of fixed and sponge boundary conditions; however they tended to generate vorticity which leads to weak spiral band-like features in the outer part of the domain, even in a stationary, symmetric storm. These were virtually eliminated when the radiation condition was used. As they were clearly an artifact of the boundary condition, they were regarded as not having any physical significance and the radiation condition was chosen. In any event, the results in the core of the cyclone are barely affected by the lateral boundary conditions used.

3.3 The Boundary-Layer of a Symmetric Storm

Three stationary, symmetric storms in a quiescent environment are considered. In the first two cases, the wind and pressure profiles are representative of a moderate cyclone with maximum gradient-level wind of 39.3 m s^{-1} at a radius of 40 km. Storm I has a moderate radial-wind profile and is the same as the case analysed using the linear model, while storm II is much more peaked, giving an annulus of zero radial M_a gradient outside the radius of maximum winds. Storm III is inertially stable throughout, but considerably more severe, with a maximum gradient wind of 59.2 m s^{-1}. Parameters used in defining the storms are defined in Table 3.1, while Fig 3.1 shows their radial profiles of gradient-level wind speed and absolute angular momentum.

3.3.1 The Inertially Stable, Moderately Intense Case

A radial cross-section through the inner part of storm I is shown in Fig 3.2. The azimuthal flow at 2 km is very close to gradient balance, so clearly supergradient flow occurs at some height everywhere outside the RMW, and to some distance inside. It is clear also that the height of the jet decreases markedly towards the centre, in agreement with the results of the linear model. The upper panels of Fig 3.3 show that the jet height is similar in the linear and numerical models, albeit with a weaker radial gradient in the former, but that the linear model predicts a substantially weaker jet. From earlier discussion, this difference is at least partly due to the omission of vertical advection. The impact of the other nonlinear terms will be discussed below. For this comparison, the drag coefficient and average turbulent diffusivity below 1 km from the full model calculation were used in the linear model, to ensure that both models represented the wind speed dependence of these parameters consistently. The choice of 1 km as an averaging height for the diffusivity was arbitrary, and other reasonable choices made only a small difference.

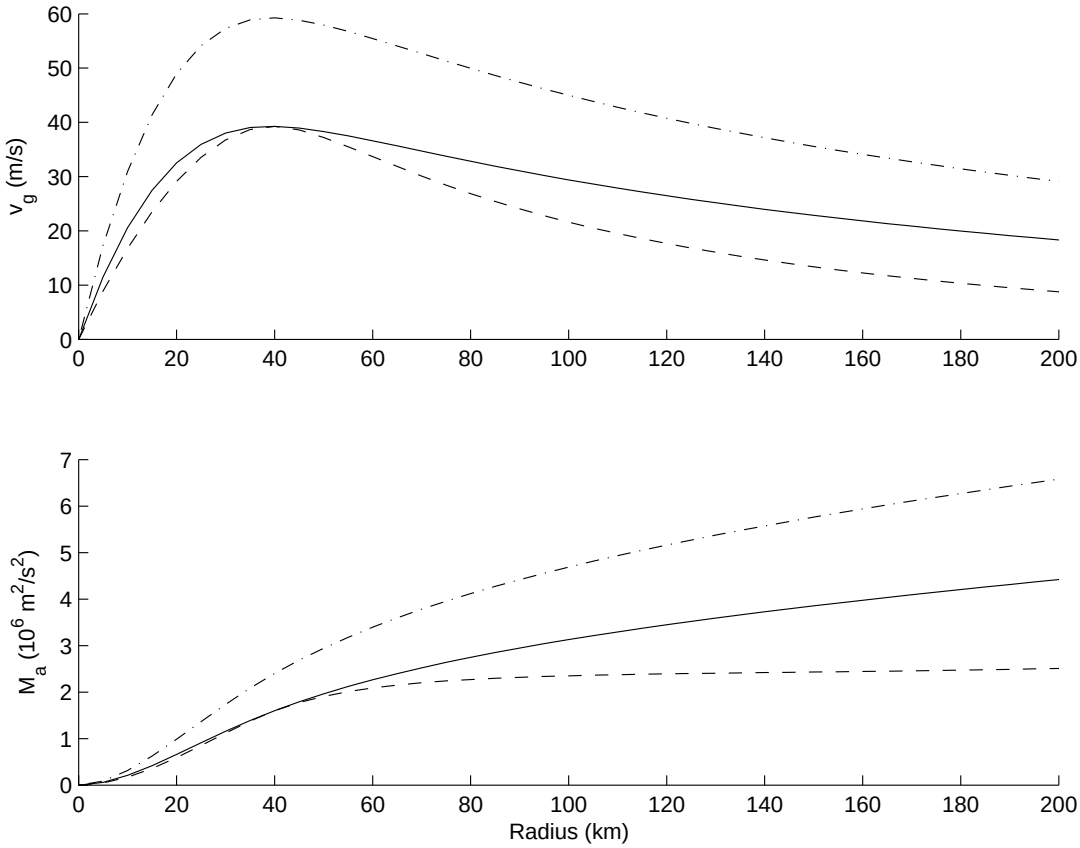

Figure 3.1 Radial profiles of gradient wind speed (top) and absolute angular momentum (bottom) for the three stationary storms defined in Table 3.1: I solid, II dashed and III dash-dotted.

Storm	Max wind	RMW	b	Latitude	Storm movement
I	39.3 m s^{-1}	40 km	1.3	15 N	0
II	39.2 m s^{-1}	40 km	2.1	15 N	0
III	59.2 m s^{-1}	40 km	1.3	15 N	0
IV	39.3 m s^{-1}	40 km	1.3	15 N	5 m s^{-1}

Table 3.1: Parameters defining the storms discussed in the text. The maximum wind is the gradient wind which would apply for a stationary asymmetric storm in the Holland (1980) parametric model. Radius of maximum winds is the radius of maximum gradient wind, and *b* is the parameter determining the "peakiness" of the parametric radial gradient-wind profile. These first four parameters determine the central pressure deficit, relative to the environment.

Also shown in Fig 3.2 are contours of M_a, which bow outwards above the jet as the wind speed decreases. The vectors of (u, w) follow the M_a contours above the jet, demonstrating that diffusive processes play only a very minor role in the angular momentum budget here. The heavy solid line shows the height at which the advection of M_a goes to 1% of its surface value at that radius. Diffusion plays a negligible role on the budget of M_a above this, but will shortly be shown to be important to the radial flow balance up to about 1 km at the RMW.

The scaling V/I for jet height proposed in (2.23), also shown in Fig 3.3, is seen to underestimate the height near the cyclone centre. This is because in the numerical model, K increases towards the centre more rapidly than the scaling (2.22), since the turbulence length-scale in the closure scheme used does not diminish towards the centre as δ_0 does. This in turn is because in the strong ascent at the core, there is no marked

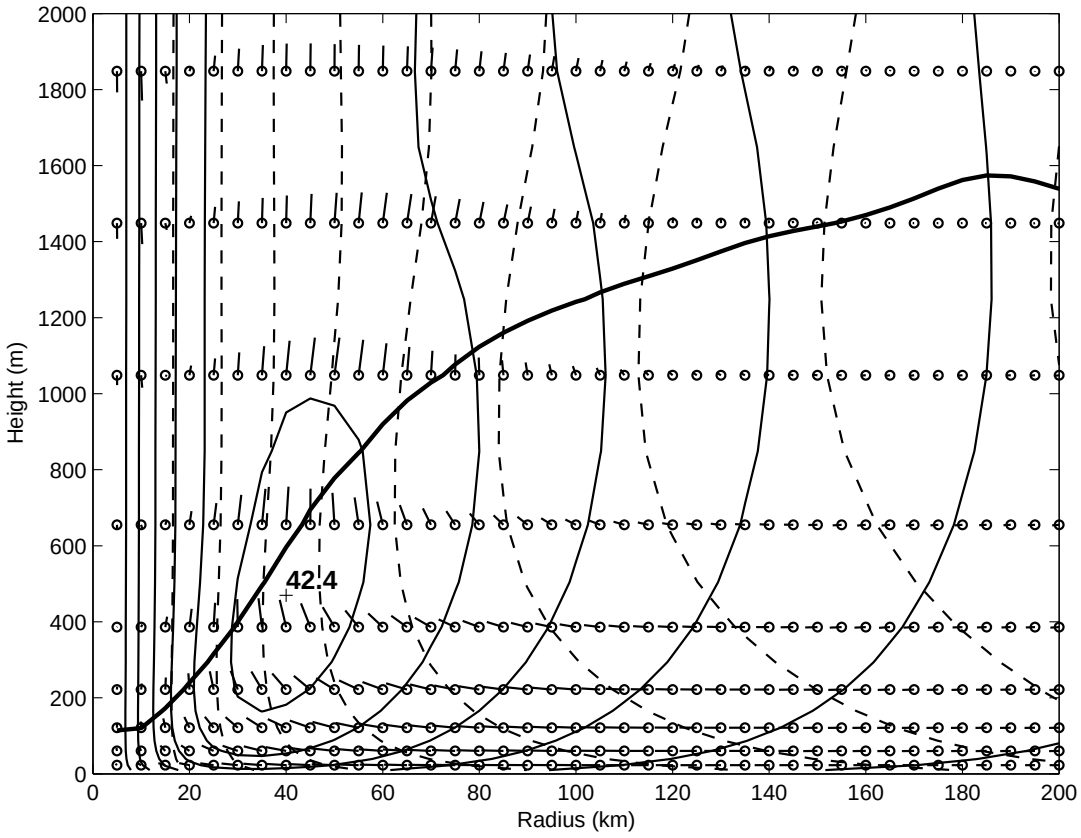

Figure 3.2 Radial cross-section through storm I. The solid light lines are contours of v, the dashed lines contours of M_a, the solid heavy line marks the top of the layer in which vertical diffusion plays a marked role in the angular momentum budget, and the vectors are of (u, w) with only every second model level shown.

increase in static stability above what has been identified as the boundary-layer top. Thus the turbulence closure is unable to identify the boundary-layer top and reduce its length scale accordingly. Clearly there is an inconsistency between the scaling argument for K and the turbulence closure implementation; which length-scale formulation is correct is less clear. If instead the turbulence length-scale had been taken to be constant with radius, then the earlier scaling argument would have given $\delta_0 \sim (V/I)^{½}$. This would tend towards zero less strongly in the core than V/I, and been more consistent with the numerical model. Neither formulation is particularly inconsistent with currently accepted boundary-layer theory; perhaps what this best illustrates is the tropical cyclone boundary-layer has some unusual aspects which require further research.

The extreme shallowing of the boundary-layer towards the centre could account for some of the large variability observed in observed wind profiles. For instance, consider profiles taken at 24 and 69 km radius, shown in Fig 3.4. Both have a gradient wind speed of 35 m s^{-1}, but are on opposite sides of the RMW. These profiles are separated by a mere 45 km, yet the jet heights differ by a factor of over two, and the corresponding 10-m winds are 28.6 and 25.5 m s^{-1} respectively, giving surface-wind factors of 0.82 and 0.73.

The updraft at the RMW is nearly twice as strong here as in the linear model, as well as being slightly less widely distributed (Fig 3.3, 3rd panel). The surface-wind factor (Fig 3.3, last panel) is very close to that derived using the linear model. Also shown is a surface-wind factor calculated relative to the wind at 700 m, which is near or below the jet height and might be expected to possibly remove some of the increase towards the centre. It is nearly constant outside the RMW, but the strong gradient inside remains.

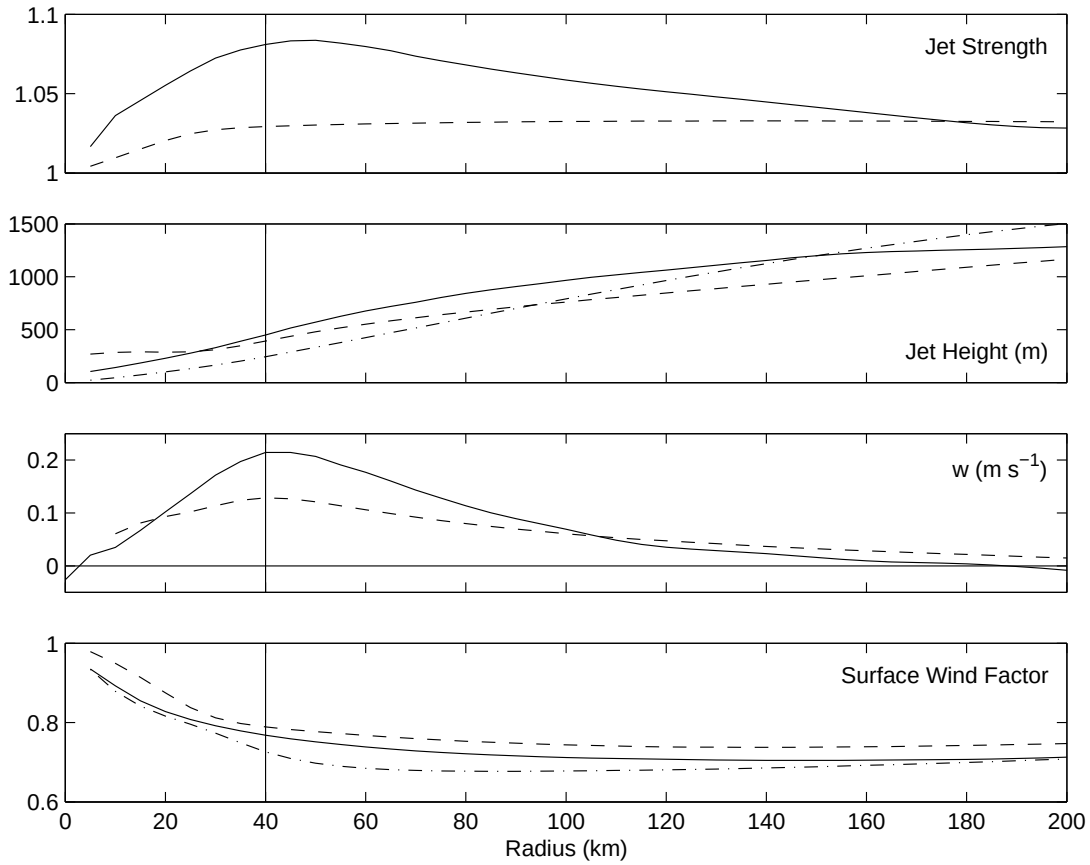

Figure 3.3 A comparison of jet strength (top) and height (second from top), vertical velocity at the top of the boundary-layer (second from bottom) , and surface-wind reduction factor (bottom), between the linear (dashed lines) and numerical (solid) models, for Storm I. The height panel additionally includes the variation of *V*/*I* (dash-dotted), which was proposed as a turbulence-parameter-free scale for the jet height. The wind reduction factor additionally shows a model derived reduction from 700 m, near or below the jet height (dash-dotted). The vertical lines in each panel are at the radius of maximum winds.

Figure 3.5 shows vertical profiles of radial and azimuthal wind for a point at the RMW of storm I. Again, the flow is nearly gradient above 1 km, and it is therefore natural to identify this as the boundary-layer top. This is a few hundred metres higher than the dark curve in Fig 3.2, which was based rather on where the influence of vertical diffusion on the angular momentum budget became negligible. It will be shown that vertical diffusion is important to the radial-wind balance up to about 1 km, so it is preferable to regard this as the top of the boundary-layer. Below this height, the inflow component increases steadily to a maximum of 9.2 m s^{-1} at 40 m height, while the azimuthal component shows a broad maximum of 42.4 m s^{-1} at 500 m, which is 8% supergradient.

The terms in the balance equations for radial velocity and absolute angular momentum are also shown in Fig 3.5. Looking first at the angular momentum, below the jet maximum the inward advection of angular momentum is balanced largely by vertical diffusion, with upwards advection playing a smaller, also weakening role. Above the jet maximum, transport of jet momentum by the eyewall updraft becomes important. This is balanced by a weak outflow of maximum strength 2 m s^{-1} at 850 m, which reverses the sign of the horizontal advection term. Note that the contribution of vertical diffusion becomes very small above 700 m height.

The budget for radial velocity at levels where the flow is supergradient is dominated by an outwards acceleration due to the imbalance in the gradient wind terms (that is, the pressure gradient, Coriolis and centrifugal terms). This is balanced largely by upwards advection and vertical diffusion of inflow, with a smaller contribution from horizontal advection. Above the jet, the gradient-wind imbalance maintains the weak outflow mentioned above – in essence, supergradient momentum carried aloft by the

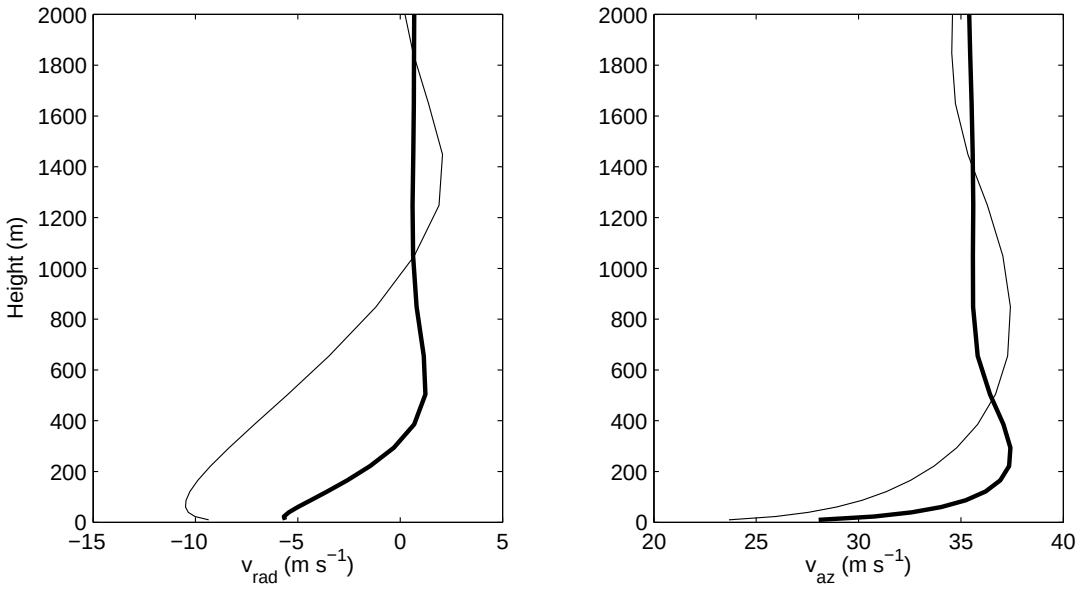

Figure 3.4 Profiles of radial (left) and azimuthal (right) wind components in Storm I, at radii of 24 km (heavy line) and 69 km (light line).

eyewall updraft is centrifuged out from the storm centre, leading to a return to gradient balance as the influence of the frictionally forced inflow recedes. A similar outflow was found by Montgomery et al. (2001) in their numerical study of vortex spindown. The role of ascent here, in helping to define the top of the boundary-layer, is in contrast to the usual role of vertical motion in boundary-layer dynamics, where subsidence produces a shallower boundary-layer with a more marked top, and emphasises the strong departures from textbook ideas of one-dimensional, horizontally homogeneous boundary-layers that are present here. Note that the model is dry and so may be underestimating the updraft strength as it does not include the buoyant forcing due to latent heat release. This would further strengthen the jet, although is probably not a major issue as the jet heights found are near or below typical cloud bases.

The budget for radial velocity at levels where the flow is supergradient is dominated by an outwards acceleration due to the imbalance in the gradient wind terms (that is, the pressure gradient, Coriolis and centrifugal terms). This is balanced largely by upwards advection and vertical diffusion of inflow, with a smaller contribution from horizontal advection. Above the jet, the gradient wind imbalance maintains the weak outflow mentioned above – in essence, supergradient momentum carried aloft by the eyewall updraft is centrifuged out from the storm centre, leading to a return to gradient balance as the influence of the frictionally forced inflow recedes. A similar outflow was found by Montgomery et al. (2001) in their numerical study of vortex spindown. The role of ascent here, in helping to define the top of the boundary-layer, is in contrast to the usual role of vertical motion in boundary-layer dynamics, where subsidence produces a shallower boundary-layer with a more marked top, and emphasises the strong departures from textbook ideas of one-dimensional horizontally homogeneous boundary-layers that are present here. Note that the model is dry and so may be underestimating

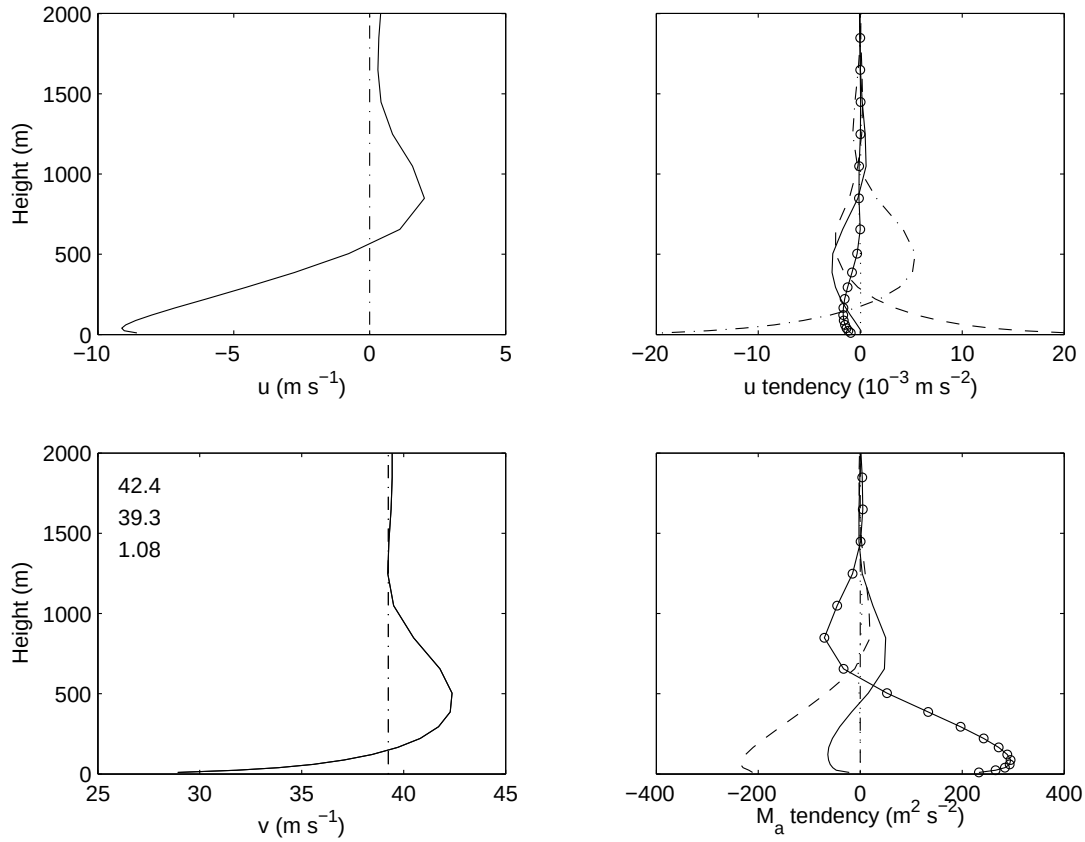

Figure 3.5 Vertical profiles of radial (top left) and azimuthal (lower left) velocity components, for a point at the gradient RMW of storm I. The dashed lines represent the gradient wind at that point. Note the strong inflow at the surface and weak outflow above 600 m, and the broad supergradient jet maximum around 500 m. Budgets of radial velocity (top right) and angular momentum (lower right) for the same point. The components are horizontal advection (solid with circles), vertical advection (solid), vertical diffusion (dashed), horizontal diffusion (dotted), and adjustment (dash-dotted). The adjustment terms for the radial velocity represent the acceleration due to the imbalance in the pressure gradient, Coriolis and centrifugal terms. For M_a, the adjustment is simply the azimuthal pressure gradient, which is zero in this axisymmetric storm. The numbers in the lower left panel are the maximum azimuthal wind, gradient wind, and their ratio, at this point.

the updraft strength as it does not include the buoyant forcing due to latent heat release. This would further strengthen the jet, although is probably not a major issue as the jet heights found are near or below typical cloud bases.

Closer to the surface, the radial flow balance is almost entirely between the gradient wind imbalance accelerating inflow, and vertical diffusion retarding it, as in the linear model. Horizontal advection is larger here than aloft, but still dominated by the other terms.

Some of the effects of the linearisation in the analytical model can also be discerned from Fig 3.5. The M_a budget at and below the jet is largely a balance between radial advection of angular momentum and its turbulent transport into the sea, as required by the linear model. Vertical advection plays a significant, but generally not dominant role there, being several times smaller than and opposite in sign to the horizontal advection. Above the jet, the vertical advection of M_a dominates the vertical diffusion, but since its sign is generally the same, it does not produce qualitatively different results to the linear model. Calculating the radial advection using $\partial M_a/\partial r$ at the top of the boundary-layer, as in the linear model, rather than within it as here, produces its largest inaccuracies near the surface. However, as the surface-wind reduction factor is here around 0.8, the relative error is not large.

In contrast, vertical advection of radial velocity is of similar importance to vertical diffusive transport in the upper part of the boundary-layer. It was the linear model's neglect of this which so weakened the jet there, and is thus the major shortcoming of that model. This is in accordance with the heuristic and mathematical arguments advanced in chapter 2, and also the scaling argument of Smith (1968)

discussed there, but note that the stronger updraft in the nonlinear model will provide an even greater enhancement of the jet. Figure 3.3 contains further evidence that it is the neglect of vertical velocity which is the major reason for the weak jet in the linear model. Outside of 140-km radius, where the numerical model has almost no updraft, the two models agree closely on the jet strength. Inside of this, where the updraft becomes significant, the numerical model produces a much stronger jet than the linear model.

The surface-wind strength is less affected than the jet by the neglect of vertical advection in the linear model, since this term tends to be is largest in the middle and upper boundary-layer where w is approaching its peak and before $\partial u/\partial z$ starts to decline. In contrast, the $u\partial u/\partial r = \partial(u^2/2)/\partial r$ term would be expected to be larger in the lower part of the boundary-layer (where the inflow is stronger) and in the inner core, where inflow is beginning to decrease rapidly towards zero at the centre. It may also be important beneath buoyant updrafts, where observational studies (e.g. Powell 1990a, Barnes and Powell 1995) have found a marked radial gradient of inflow. It is therefore more important to the strength of the near-surface winds than to the strength of the jet, and leads to weaker near-surface winds outside the radius of maximum inflow, and stronger ones inside, than would apply if it were omitted. Near the surface, the radius of maximum inflow is about 60 km, and so this term is largest in the vicinity of the RMW. However, the inflow budget there is shown in Fig 3.5 to be dominated by the vertical diffusion and gradient imbalance terms, with horizontal advection being much smaller. So neglect of this term in the linear model does not produce substantial errors in the near-surface flow in this case.

In summary, the analytical formulae for jet height and surface-wind factor derived from the linear model are applicable to the full model, as the nonlinearities are

not dominant influences to these. However, vertical advection of inflow contributes strongly to jet strength, which is substantially under-predicted by the linear model.

3.3.2 Height scales in Storm I

Although the linear model substantially under predicts the jet strength in regions of strong updraft, relative to the numerical model, it was shown above that there was substantially better agreement with the height. The linear model boundary-layer depth scale δ_0 ignores vertical advection. However, w increases from 0 at the surface to a maximum at the boundary-layer top. Thus one could argue that adding vertical advection to the physics does not therefore introduce any fundamentally new depth scale, but rather modifies that already pertaining, and so the linear-model scale for jet height is perhaps applicable here. Alternatively, in the extension of the linear model in section 2.3.6, where a constant vertical velocity was imposed, it was shown that the stronger jet found in an updraft could also be interpreted as a modification of the spiral, where the oscillation scale decreases and decay scale increases. To test this, curves of the form

$$\sqrt{\beta/\alpha}\ u + iv = A\ \exp(-z/\delta_{decay})\ \exp(iz/\delta_{osc}) \qquad \textbf{(3.6)}$$

for complex coefficient A and real depth scales δ_{decay} and δ_{osc}, were fitted to the wind profiles from the numerical model. Sample modelled and fitted hodographs are shown in Fig 3.6, which show both the essentially spiral character of the numerical results, as well as the very good fit to them of such curves. The corresponding decay and oscillation depth scales are shown in Fig 3.7, with the predicted difference in the core region being apparent. The vertical velocity at a height of 1 km is also shown, and it is remarkable that the region where the decay length is longer than the oscillation depth corresponds very closely with the region of significant updraft, in agreement with the above discussion

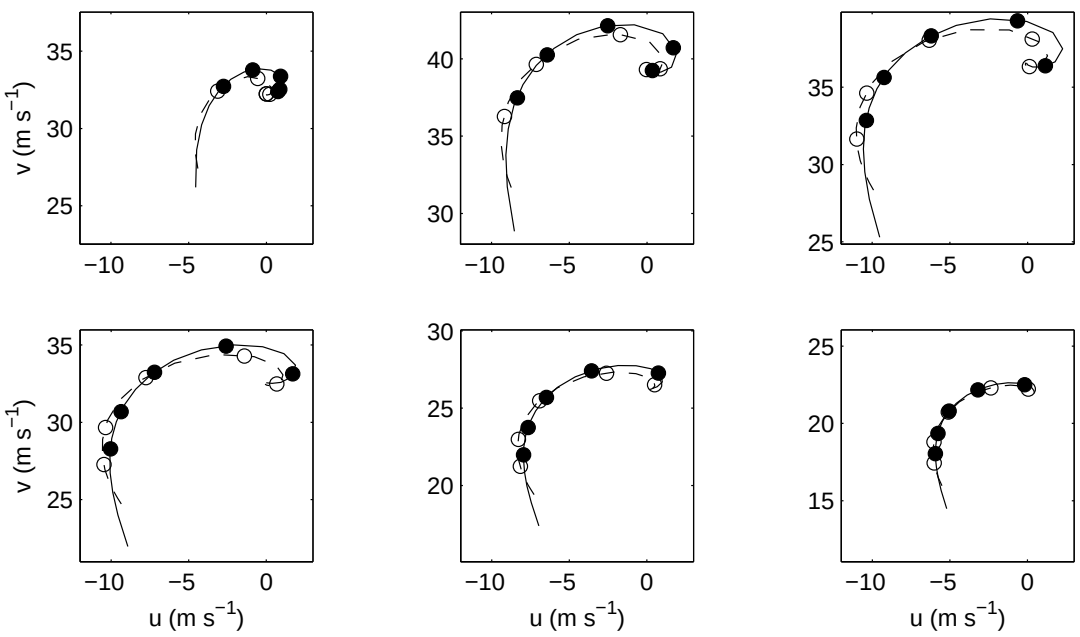

Figure 3.6 Hodographs of modelled (solid line with filled circles) and fitted (dashed with open circles) wind profiles in Storm I at radii of (from top left) 20, 40, 60, 80, 120 and 160 km. Circles on the hodographs indicate heights of 100, 200, 400, 800 and 1600 m.

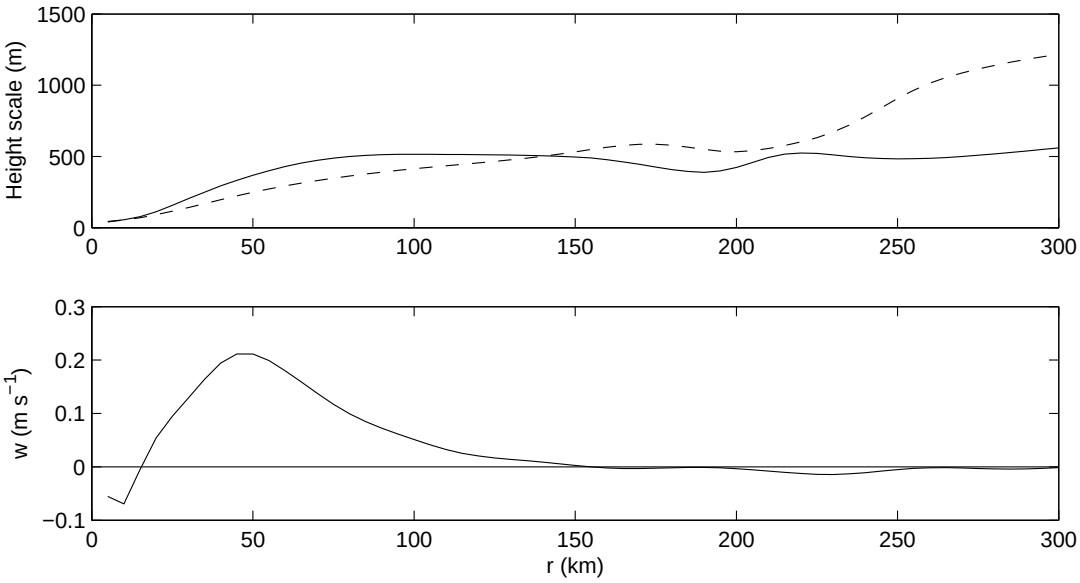

Figure 3.7 Top: Radial profiles of decay (solid) and oscillation (dashed) height scales. Bottom: Vertical velocity at 1 km

Empirical curves of the form (3.6) thus describe well the profiles in the numerical model. The decay length-scale is longer (shorter) than the oscillation scale, in an updraft (downdraft), in agreement with the analysis in section 2.5. This thus provides further confirmation of the importance of the vertical velocity in defining the shape of the wind profile in the tropical cyclone boundary-layer. It also demonstrates that the introduction of more complicated physics here does not produce major changes in the basic shape of the profiles.

3.3.3 Comparison to the nocturnal jet

It will now be shown that the jet here is distinct from the familiar nocturnal jet. The latter has been widely studied, with many simulations of data from, for example, the Wangara experiment (Clarke et al. 1971), showing the effect. Here, the comparison will be with the simulation of Mellor and Yamada (1974, henceforth MY74) as they use a similar turbulent closure to the present model, and include figures of all the relevant terms.

Figure 3.8 shows the Richardson number Ri, the turbulence kinetic energy (TKE), and the turbulent diffusivity for momentum for the same RMW point in Storm I. Note firstly that Ri is very small in magnitude through the boundary-layer, suggesting shear production will dominate the TKE budget, and is in fact slightly negative at and below the jet. This is completely contrary to the situation in the nocturnal jet (MY74 Fig 5), where strong stabilisation and buoyant suppression of turbulence are necessary for the decoupling which then allows the inertial oscillation which produces the jet. The TKE decreases from a surface maximum to become nearly zero at about 1 km, the top of the boundary-layer, so the jet here occurs entirely within the boundary-layer. Again, this is distinct to the nocturnal jet, which occurs at the top of the nocturnal boundary-layer,

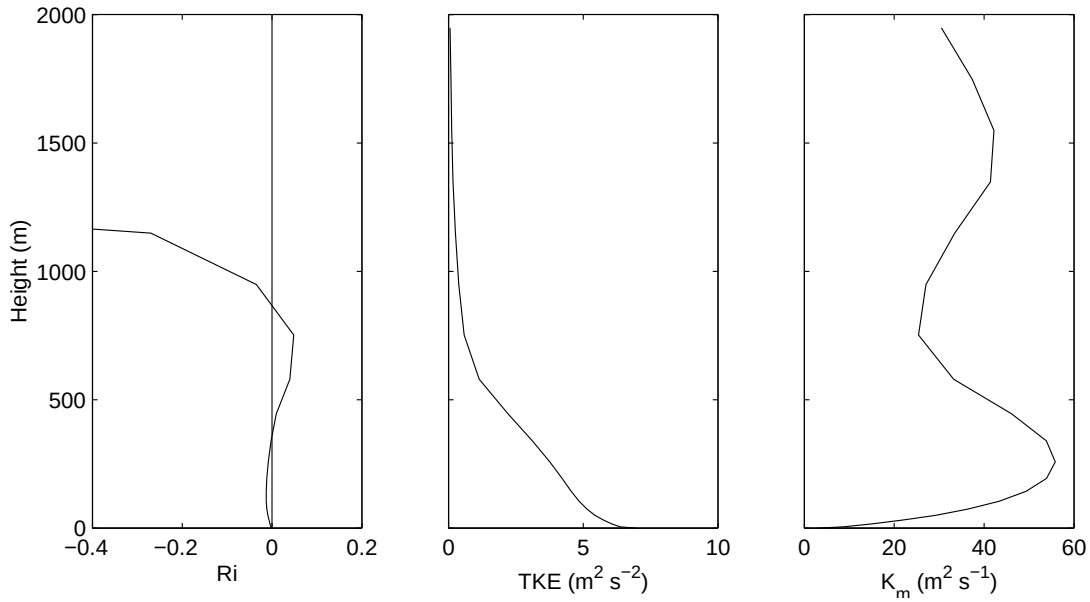

Figure 3.8 Vertical profiles of Richardson number (left), turbulence kinetic energy (centre) and turbulent diffusivity for momentum (right), for the same eyewall point in Storm I as Fig 3.5.

where TKE has become essentially zero (MY74 Fig 6). Finally, observe that the turbulent diffusivity has a maximum immediately below the jet. This maximum occurs because the diffusivity in the level 2 1/4 closure is the product of the square root of the TKE, the master length-scale, and a stability dependent term. Their respective height variation through the boundary-layer is to decrease to nearly zero, to increase from zero and to be nearly constant, with the net result being a maximum about halfway up the boundary-layer. This confirms that the jet is in a region of strong turbulent transport, and is therefore not a consequence of frictional decoupling. The negative values of Ri, and local maximum in K_M, near 1500 m, are a consequence of weak static instability and weak shear well above the boundary-layer in the numerical model, and are of no dynamical significance. Note, however, that Black and Holland (1995) found evidence of a jet due to surface cooling and low level decoupling in the periphery of Tropical Cyclone Kerry (1979). The large positive values of Ri they found beneath the maximum suggest it may be distinct to the one being analysed here.

3.3.4 An Inertially Stable, Intense Storm

Turning to the more intense storm III, the jet is again most marked just inside of the gradient RMW, where at 65.8 m s^{-1} it is 11% stronger than the gradient wind. Figure 3.9 shows vertical profiles of angular momentum and radial velocity at the RMW, as well as the terms in the budget equations. These are similar in appearance to those for the weaker storm I, albeit with considerably larger values. One significant change is that the outflow above 1 km has become considerably more marked. The strong upwards advection of M_a responsible for this is partly due to the larger vertical gradient of M_a associated with the stronger jet, but more to the fact that the eyewall updraft has doubled in strength, giving much stronger vertical advection in this more intense storm. The other significant nonlinear term, $u\partial u/\partial r$, has also increased in relative importance here,

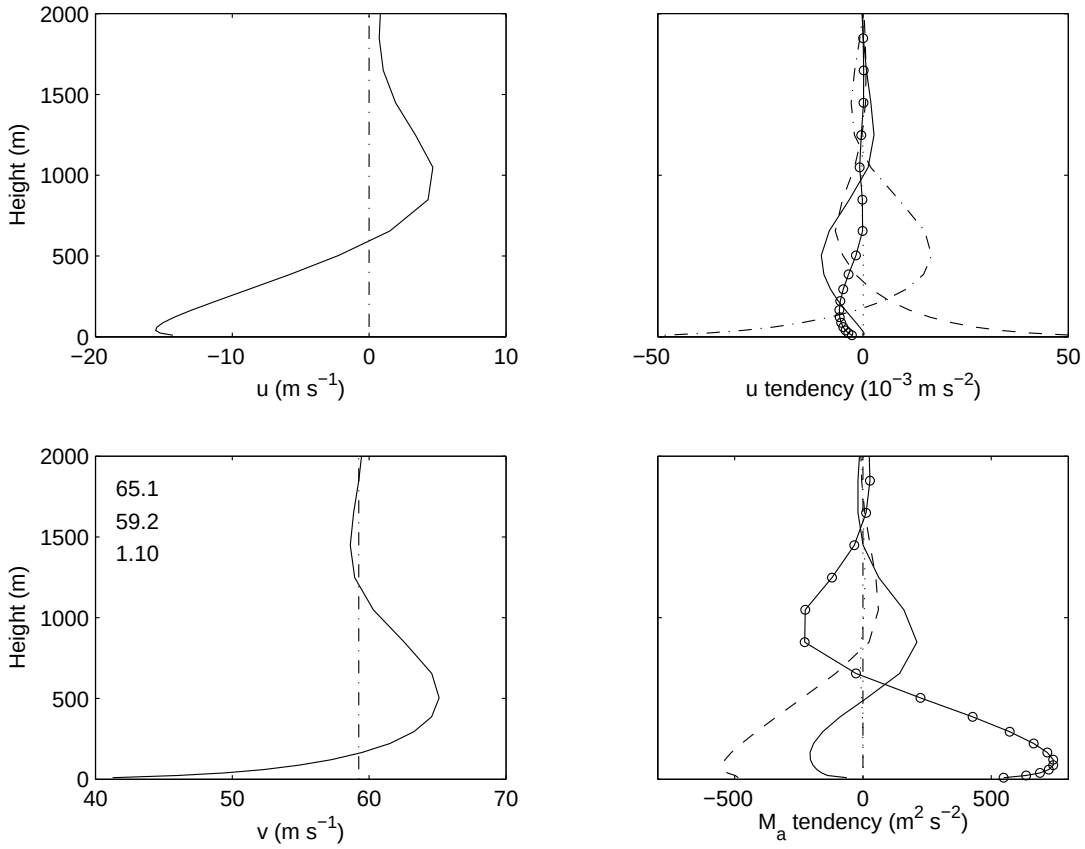

Figure 3.9 Flow components and budgets at the RMW of the severe storm III. Meaning of curves is the same as Fig 3.5.

although is still dominated by the diffusion and adjustment terms. Thus, as before, the main shortcoming of the linear model is its neglect of vertical advection.

The analysis so far has strongly suggested that the radius of maximum winds is a highly favourable location for low-level jet occurrence, due to the sudden increase in inertial stability allowing a strong updraft there, and the increased radial gradient of M_a[5]. Tropical cyclone rainbands are also associated with strong updrafts, and observational studies (Powell 1990a) have showed that the strong convergence beneath the band is associated with enhanced inflow on the outer side of a band, and weak or absent inflow on the inward side. Also, the along-band wind maximum sometimes observed would give an enhanced radial gradient of M_a of the outside of the band. It has been shown above that inflow across such a gradient will generate a jet, and that an updraft will enhance it. It is therefore reasonable to speculate that rainbands may be a favourable location for jets. Note, however, that the mechanism described here can produce supergradient flow anywhere there is inflow and inertial stability, and also that the observational record is equivocal. While Moss and Merceret (1975) found their jet in such a location, Powell's analysed along-band flow (1990a, his Fig 13b) shows a maximum at about 500 m extending from about 5 km outside, to at least 20 km inside, of the band. Similarly, of the three stepped-descent profiles he presents (his Fig 15), the two taken inside the band show a jet at about 500 m, while the one taken outside the band show no evidence of a jet. Clearly, the rainband scale structure of the jet requires further research.

3.3.5 The Inertially Neutral Case

The radial strength and height of the jet for the peaked wind profile, storm II, where gradient-level absolute angular momentum is essentially constant with radius for

[5]These are of course related, through $I^2 = r^{-3}\,\partial M_a^2/\partial r$.

several hundred kilometres outside of the radius of maximum wind, are shown in Fig 3.10. With no possibility for radial advection of angular momentum outside of 60-km radius, the jet is confined to the immediate vicinity of the RMW, where the steep, almost step-like, gradient in M_a produces a marked jet with azimuthal wind component 48.3 m s^{-1}, which is 25% supergradient, near 500 m just inside the gradient RMW. The updraft is likewise now restricted to the vicinity of the RMW, and the surface-wind factor shows a peak here associated with the strong jet. In contrast to the previous cases, the linear model shows little agreement here, with the vertical velocity in particular being a poor representation of reality. This is not unexpected, as the linear model is outside its range of validity in the annulus of inertial neutrality.

Vertical profiles and budgets of u and M_a at the RMW for this storm are shown in Fig 3.11. Although the signs of the various terms and the general shapes of their profiles are similar to those for storm I, their relative magnitudes and depth scale have changed dramatically. Both the strength of the jet and the strength of the near-surface inflow have more than doubled relative to storm I. This is accompanied by substantial increases in the contribution from nonlinear advective terms in the budgets. In particular, vertical advection is now approximately as important as vertical diffusion in balancing the inwards advection of angular momentum below the jet, while above there is now substantial outflow above the jet as the strongly supergradient flow in the updraft returns to balance. In the radial flow budget, vertical diffusion is of relatively minor importance away from the surface, and the outwards acceleration due to gradient adjustment is balanced largely by upwards advection of inflow.

This great increase in the importance of vertical advection is largely due to the much stronger updraft in this storm. Indeed, the radial distribution of vertical velocity,

shown in Fig 3.10, is quite different in the two storms, with the much stronger eyewall updraft in storm III being surrounded by a ring of weak subsidence, as was hinted at in the analysis of the linear model. Since the storm is symmetric, the horizontal divergence associated with this subsidence requires that the inflow increase inwards at least as rapidly as $1/r$. Thus the near-surface inflow at the RMW here is twice as strong as in Storm I.

The dynamics behind this rapidly accelerating inflow are shown in Fig 3.12, which shows wind components and budgets at three times the RMW, near the peak subsidence. Frictional destruction of M_a near the surface produces subgradient flow there, and consequently a strong inwards acceleration in the adjustment term in the radial-wind budget. Except very near the surface, this inwards acceleration is balanced dominantly by the $u\partial u/\partial r$ term rather than by friction. From a Lagrangian point of view, the imbalance in the adjustment terms directly accelerates the air parcels inwards. In the inertially stable storm, the inflow produced sufficient horizontal advection of M_a to balance the frictional destruction. While storm II here has zero radial gradient of M_a at gradient level, the lighter winds near the surface increase the relative importance of the $fr^2/2$ term over rv and allow a weak near-surface radial gradient of M_a. The accelerating inflow thus provides sufficient radial advection of M_a to largely balance frictional destruction. Downwards advection by the subsidence makes a further contribution, which is of similar magnitude to horizontal advection above 1 km.

The stronger inflow here, compared to storm I, appears to be similar to the differences noted between Hurricanes Hilda and Inez (Hawkins and Rubsam 1968, Hawkins and Imbembo 1976). Inez was a relatively small storm with a peaked wind profile and therefore similar to Storm II, while Hilda was larger with a flatter wind

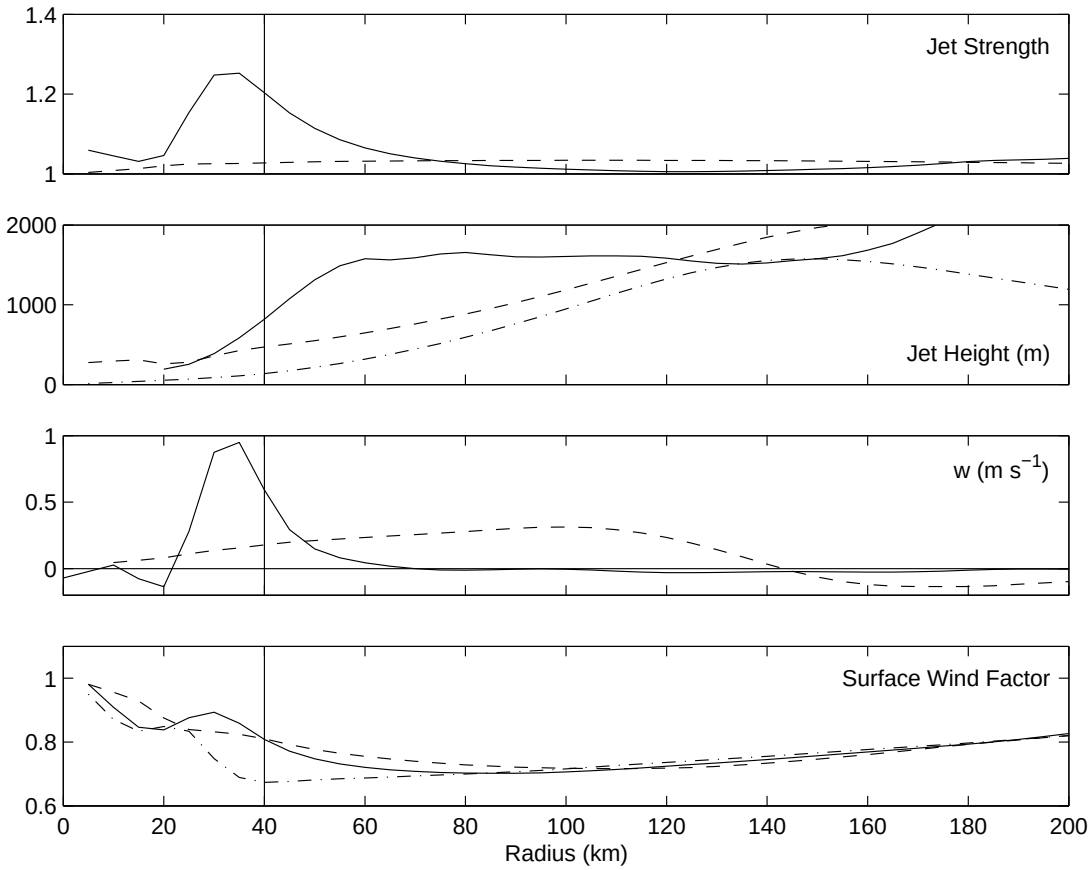

Figure 3.10 The same as Fig 3.3, except for the inertially neutral Storm II.

profile. The inflow in Inez was analysed to be 2 – 3 times stronger than that in Hilda, consistent with these results.

In summary, frictional destruction of M_a outside the RMW produces inflow. In the inertially-neutral outer core of this storm, only weak advection of M_a then arises, so the inflow continues to accelerate, leading to low-level divergence and subsidence. When the inrushing air encounters the inertially stable core, overshoot (shown by the $u\partial u/\partial r$ term in Fig 3.11) leads to a very strong jet and near-surface winds. Gradient adjustment of these strong winds eventually stops the inflow, with a strong updraft resulting.

The much stronger inflow in this case can be related to the results of the balanced vortex diagnostic models (e.g. Willoughby, 1979). A key finding of these was that the strength of the radial response to forcing in an axisymmetric tropical cyclone was determined by the inertial stability. The much stronger inflow in the inertially neutral Storm II can be regarded as a consequence of this. Note, however, that the balanced models do not produce supergradient flow since they are by definition balanced, and that where they produce outflow above a layer of boundary-layer inflow, it is because their high background static stability vertically constrains a circulation whose outwards branch's role is to satisfy continuity. In contrast, the outflow above the jet found here is a direct result of gradient imbalance. The boundary conditions here impose no stability constraint on upwards motion above the boundary-layer, and mass is allowed to exit the top of the model. This is appropriate, since in a real cyclone latent heat release would be occurring in this updraft, and while the balanced vortex modellers have been concerned with the cyclone-scale response to various forcings, the focus here is on resolving the details of the boundary-layer response to forcing by the cyclone.

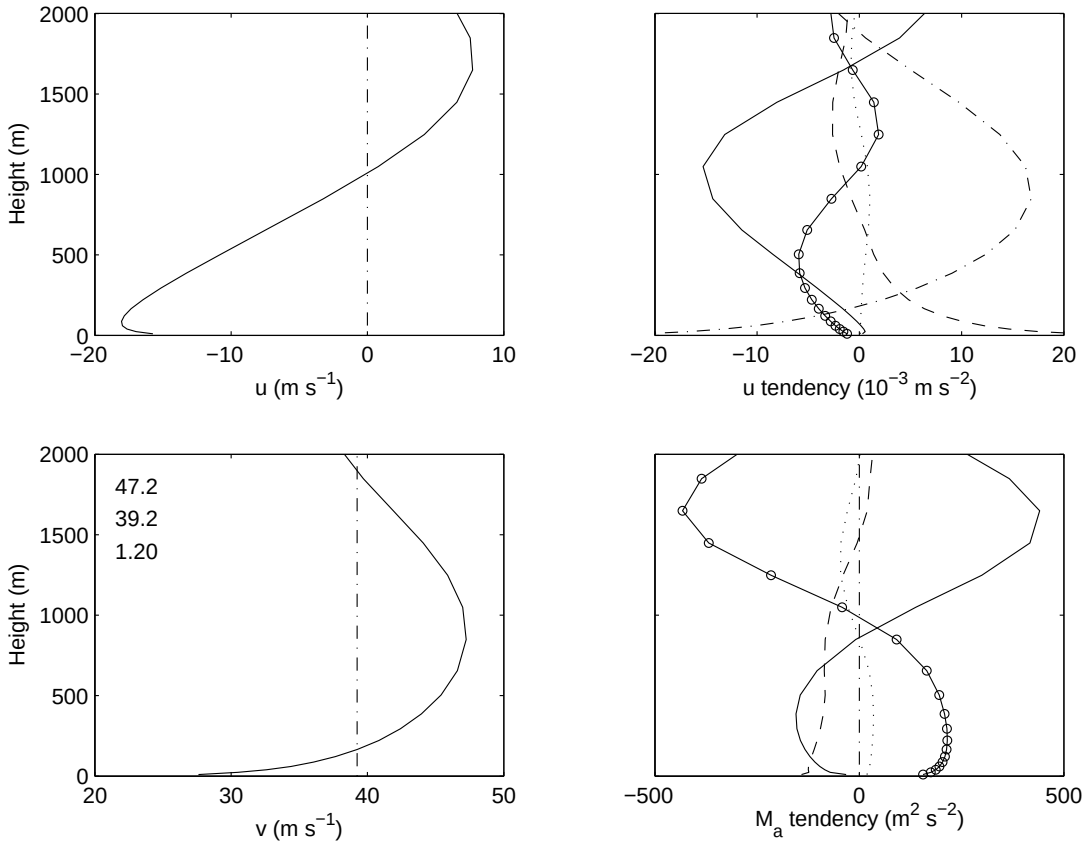

Figure 3.11 Flow components and budgets at the RMW of the inertially neutral storm II. Meaning of curves is the same as Fig 3.5.

In summary, this storm is quite different to the inertially stable case. The jet is much stronger, but confined to the immediate vicinity of the radius of maximum winds. The updraft there is stronger than before, and surrounded by an annulus of subsidence, while the inflow is markedly stronger. The dynamics are markedly different, in that nonlinear processes completely dominate those in the linear model. The poor comparison between the numerical and linear model in Fig 3.10 is thus not surprising.

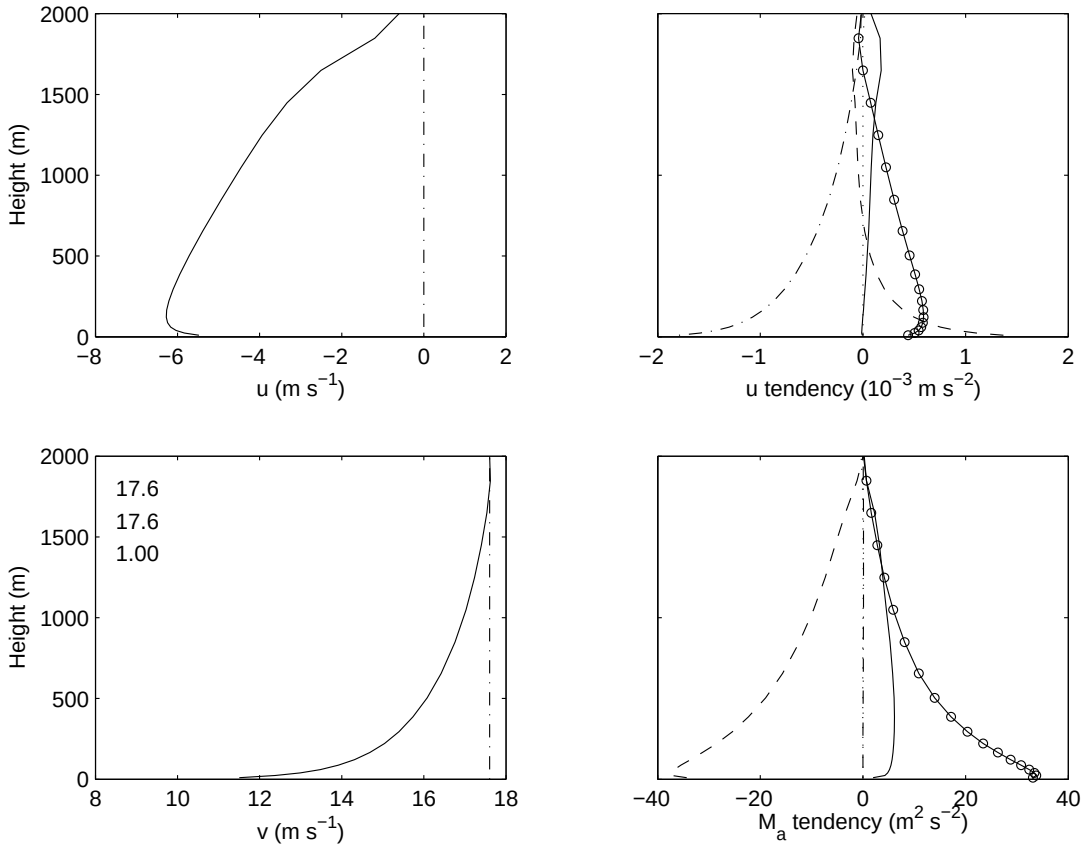

Figure 3.12 Flow components and budgets for a point at three times the radius of maximum winds in Storm II. Meaning of curves is the same as in Fig 3.5.

3.4 The Effect of Cyclone Movement

3.4.1 Boundary-Layer Flow in a Translating Cyclone

The flow in a moving storm will now be illustrated, using storm IV, which is identical to storm I, but embedded in and translating with a 5 m s^{-1} easterly flow. It thus corresponds to the moving storm case of chapter 2.

The near-surface storm- and earth-relative wind fields for this storm are shown in Fig 3.13. The maximum storm-relative azimuthal wind is located in the left-forward quadrant, with the strongest winds just inside the radius of maximum gradient-level winds. This is downstream of the maximum storm-relative inflow, in the right-forward quadrant. The maximum earth-relative azimuthal and inflow components lie slightly to the right of the front and to the right of the track, respectively. This distribution is highly consistent with the linear model, as well as the observational studies cited earlier.

The updraft (Fig 3.14) is strongest in the right-forward quadrant, with weak subsidence opposite, in good agreement with the linear model. However the asymmetries are markedly stronger and located closer to the RMW than in the linear model, while the anticyclonic spiral character of w is more marked. The sense of this spiral is opposite to that for a rain band, and it is confined to the vicinity of the RMW. Thus it should not be interpreted as a forcing for a rain band, but rather an eyewall asymmetry similar to that in the (u_{-1}, v_{-1}) component of the linear model. The surface-wind factor is in close agreement, although a little weaker, than was found in the linear model. However the spatial variability is qualitatively very similar, and the quantitative differences are partly due to the use of different values for the drag coefficient and diffusivity in the two models.

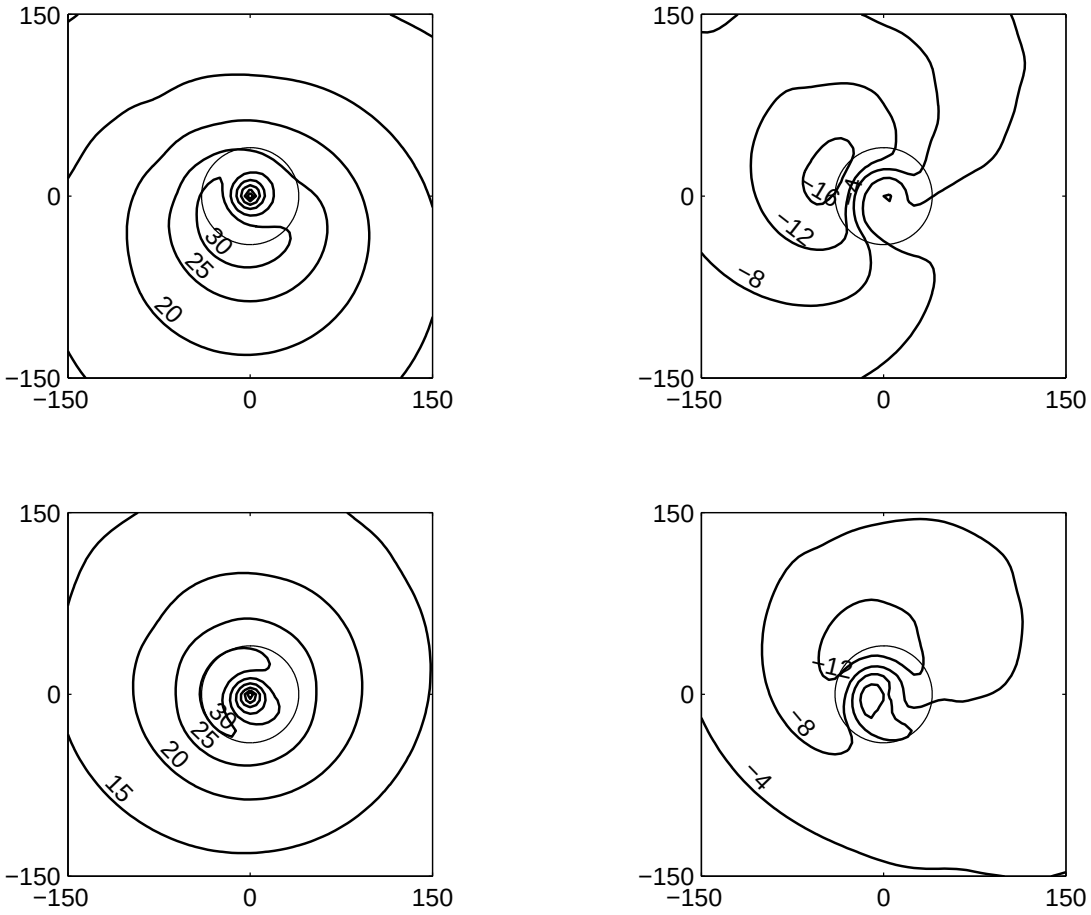

Figure 3.13 Storm-relative azimuthal (top left) and radial (top right) flow, and earth-relative azimuthal (lower left) and radial (lower right) flow, at 10 m in Storm IV. The light circles in each panel indicate the radius of maximum winds, the horizontal scale is in kilometres, and the wind speeds in m s^{-1}.

The distribution and relative magnitude of the jet are also shown in Fig 3.14. The virtual obliteration of the jet to the right-rear of the storm is in very good agreement with the linear model. However, the structure to the left-front of the storm is rather different. The strongest jet is in the left-forward quadrant just inside the radius of maximum gradient winds, where it is 28% supergradient, or over three times what was found in the stationary nonlinear case. This large value will be shown later to be partly due to the conjunction of some favourable nonlinear factors, combined with the basic asymmetry described by the linear model. The maximum jet location is slightly downwind of where Shapiro (1983) found the maximum winds (which were also supergradient) in his slab model, although some care is needed in comparing the maximum wind within a profile here, with Shapiro's mean wind in a slab boundary-layer. There is a steep radial gradient of jet height around here, but the height of the maximum jet is 540 m.

A subtlety arises in calculating the jet strength and surface-wind factors. So far, these have been calculated relative to the gradient wind, in earth-relative coordinates. However, in practice, the gradient wind is hard to measure and it might be preferred to use, for instance, an aircraft measurement at 2-km altitude. For the stationary storm, the boundary-layer is shallow and there is no practical difference. However, the components (u_{-1}, v_{-1}) in the linear model had a distinctly larger depth scale, and examination of the flow near 2 km in the numerical model shows a similar but much larger wave number one asymmetry, of amplitude ±6 m s^{-1}. This is large enough to have a significant effect on the patterns of surface-wind factor and jet strength if they were calculated relative to this, rather than to the gradient wind. Figure 3.15 shows the asymmetric earth-relative azimuthal flow at 2 km from the numerical model, and the surface-wind factor and jet strength calculated relative to the total wind (in stationary coordinates) at this level, which should be compared to those in Fig 3.14. The latter two fields show an area of

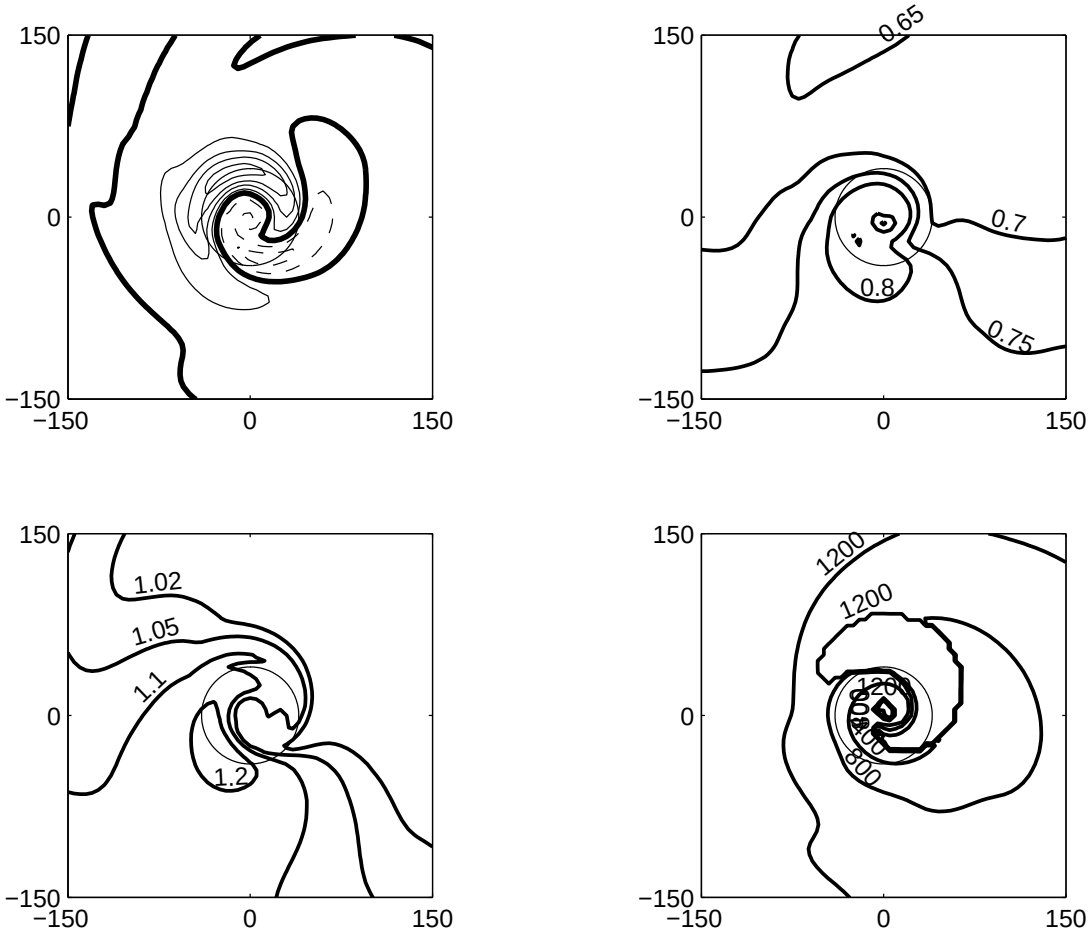

Figure 3.14 Vertical velocity (upper left) at 2 km for the leftwards moving storm IV (zero contour heavy, negative contours dashed, contour interval 0.2 m s^{-1}). Ratio of the earth-relative 10-m wind speed to the earth-relative gradient wind speed, for the same storm. Jet strength (lower left, relative to the earth-relative gradient wind speed) and height (lower right), for the same storm.

enhanced values extending into the right-rear quadrant, precisely where the asymmetric *v* component is acting to reduce the net 2-km azimuthal component. Comparison on this basis also reduces the apparent strength of the surface and jet flows in the left-forward quadrant, where the asymmetric *v* component increases the 2-km wind. This suggests that for practical use, different factors may be required depending upon whether one is trying to reduce gradient winds, or observations, to the surface.

In the linear model, the flow components due to the motion were independent of the symmetric component. While interaction between these components would be expected in a full model, the symmetric part nevertheless provides a good starting point for understanding the flow here. The azimuthal average around the RMW of the wind components and their budgets is shown in Fig 3.16. The strength of the jet and near-surface inflow have increased by 0.5 m s^{-1} and 1 m s^{-1} respectively from the stationary case, while the maximum azimuthal-mean updraft at 1 km (not shown) has gone from 0.21 m s^{-1} to 0.29 m s^{-1}. Similarly, the jet height, and terms in the momentum budgets, are in very good agreement with the stationary case. The major difference is that the supergradient flow extends further above the jet core than in the stationary case. However, the overall picture of vertical advection and turbulent transport of inflow being necessary to maintain the inflow against gradient adjustment of the supergradient jet is still valid.

The asymmetries in the jet can be understood either in terms of the linear model, or in terms of enhanced inflow forcing (associated with storm asymmetries) allowing stronger supergradient flow to develop. Here, both interpretations are given. At the RMW at the front of the storm (Fig 3.17), low-level inflow is maintained in the presence of a 23% supergradient flow by both horizontal and vertical advection. The role of

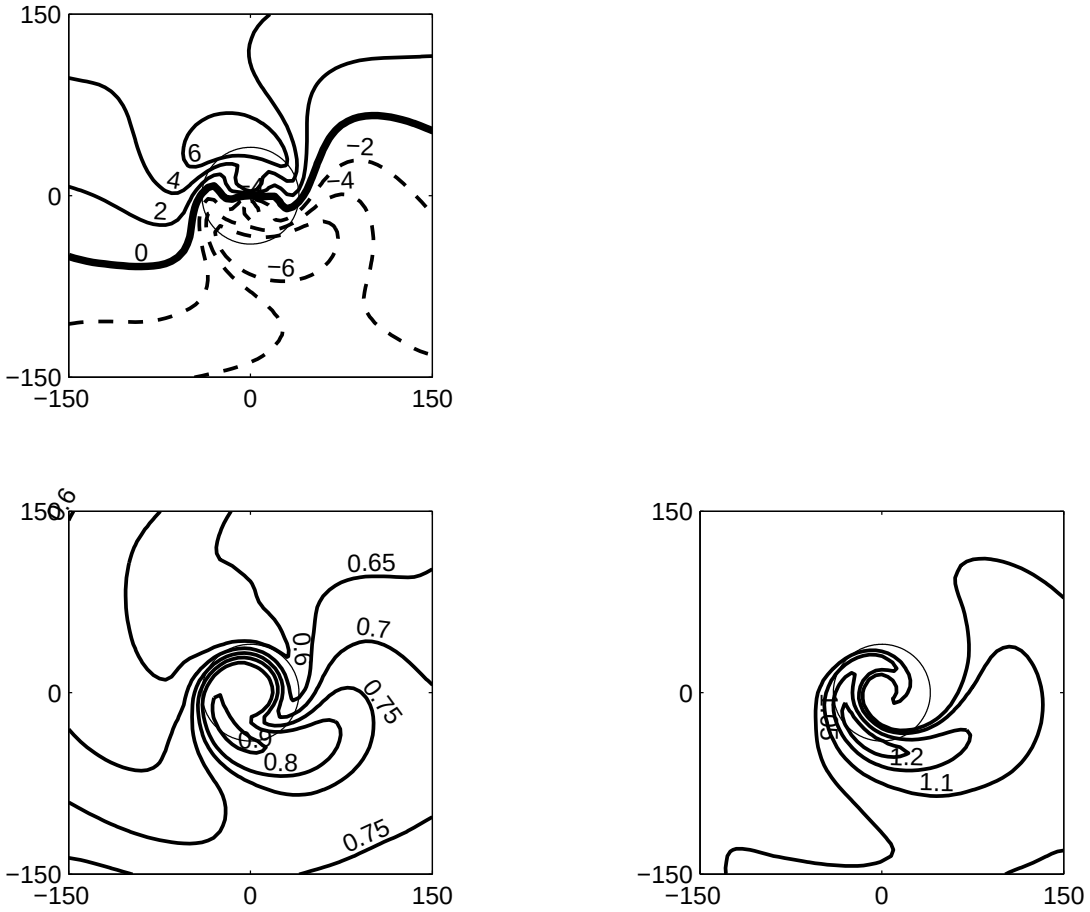

Figure 3.15 The asymmetric component of the azimuthal flow at 2 km (top), the ratio of the surface-wind speed to the 2-km wind speed (lower left), and the jet strength relative to the 2-km wind speed (lower right), for Storm IV. Earth-relative wind speeds are used in all panels.

vertical diffusion, in contrast to the stationary case, is virtually negligible here. The horizontal advection is dominated by the azimuthal advection of the asymmetric part of u (not shown), a term which is included (in linearized form) in the linear model. The inflow layer is about 1 km deep, the substantial outflow aloft being associated with a sign reversal of the angular momentum horizontal-advection term and a gradual return to gradient balance above the jet. Comparison of the symmetric and full components of the radial-wind shows that the inflow is stronger below, and the outflow stronger aloft, than in the azimuthal average. The azimuthal wind component here is almost everywhere stronger than its azimuthal average. Both of these are qualitatively consistent with the flow components (u_{-1}, v_{-1}) for the linear model shown in Fig 2.5.

To the left of the storm, (Fig 3.18), the jet is lower and slightly weaker. Inflow is nearly absent except for very near the surface. Here, the decline in the updraft, and also the reversal of the sign of the advection of radial flow aloft, have allowed the flow above 1.1 km to become subgradient. The supergradient flow closer to the surface is maintained by azimuthal advection around from the front of the storm, rather than by inwards advection. The jet is thus weakening here, and may be regarded as the decaying remnants of the maximum jet found in the left-front quadrant. Again, the differences between the flow here and the azimuthal average are in qualitative agreement with the linear model.

Behind the storm (Fig 3.19), no obvious jet is present below 2 km and the flow below 1300 m is both subgradient and inwards, with the reverse applying aloft. The weak inflow, and azimuthal advection, both contribute to maintaining the azimuthal flow against frictional dissipation, but are insufficient to generate supergradient flow below 1 km. Only aloft is this marginally present. The flow relative to the symmetric component

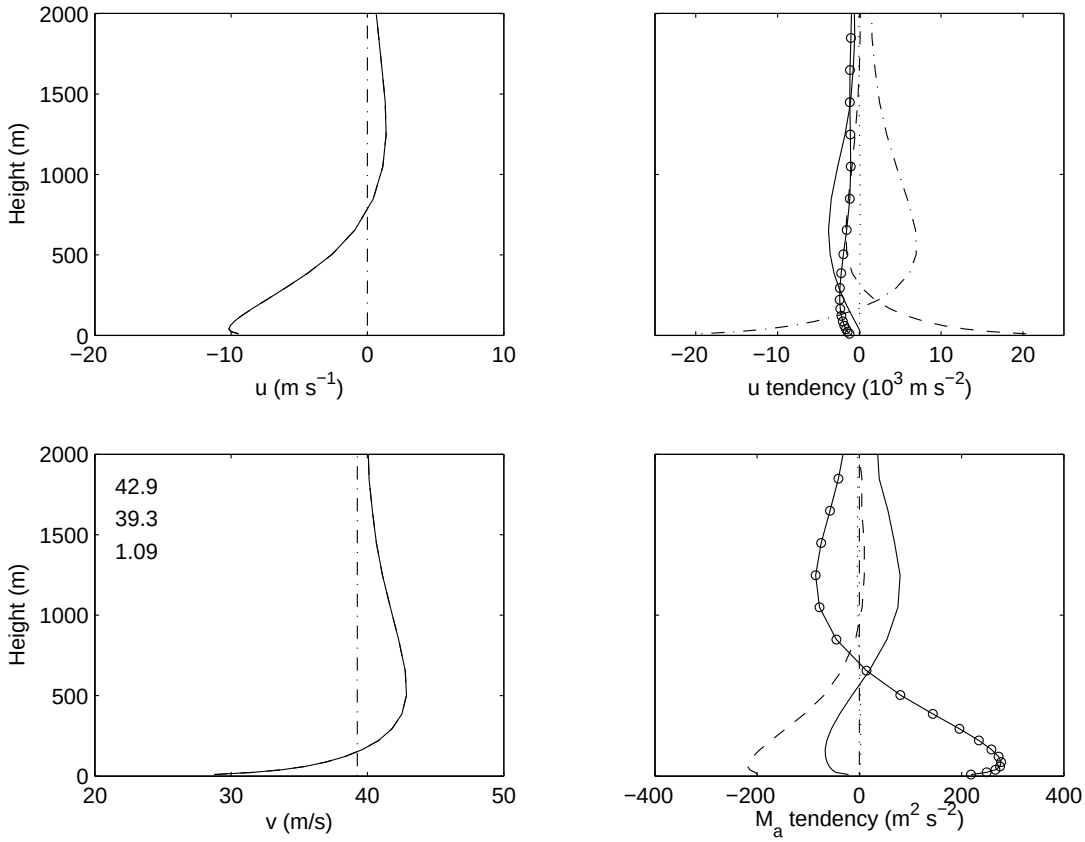

Figure 3.16 Flow components and budgets for an azimuthal average around the radius of maximum winds in Storm IV. Meaning of curves is the same as in Fig 3.5.

is now virtually reversed from that in front of the storm, and is therefore again in agreement with that found in the linear model.

Finally, to the right of the storm (Fig 3.20) the flow is broadly supergradient from 400 m to above 2 km, accompanied by strong inflow. In one sense, this flow, although supergradient, is not sufficiently confined in the vertical to be regarded as a jet. Here, the asymmetric components are quite close to being the opposite of those to the left of the storm, and thus detract from, rather than sharpening, the low-level maximum in the symmetric component. Remarkably, the terms in the angular momentum budget virtually vanish above 800 m. However, this is a somewhat misleading picture, as the radial and azimuthal components of the horizontal advection (not shown) are both of order 100 $m^2\ s^{-2}$, and cancel. This could be regarded as a characteristic of the inertial wave discussed in chapter 2. Alternatively it can be interpreted in terms of the linear model, as an area where the peaks and troughs in the symmetric and asymmetric components cancel, as therefore do the various terms in the budgets, giving the apparently near-zero terms above about 800 m.

It is clear from Figs 3.17 – 3.20 that the asymmetric components of the flow are generally greater than the symmetric part near 2 km. This is consistent with the linear model, as the depth scale δ_{-1} of the dominant asymmetric component is almost twice that for the symmetric component, δ_0.

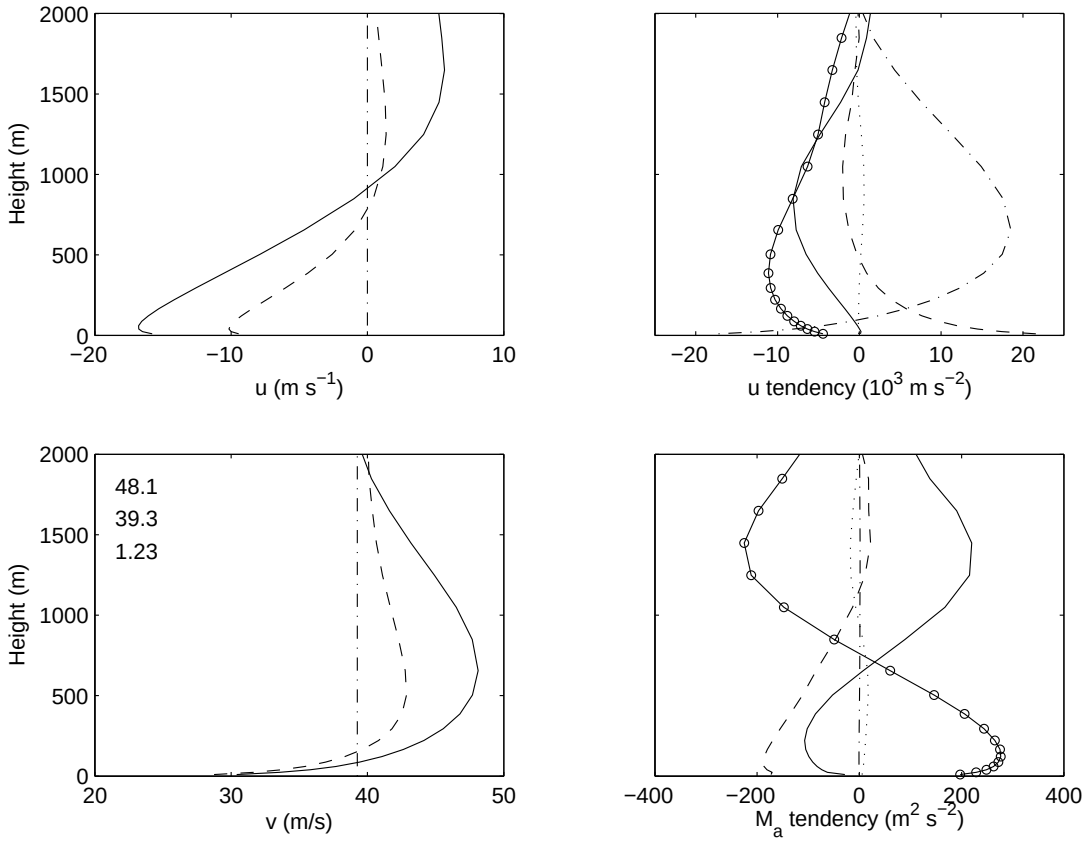

Figure 3.17 The same as for Fig 3.16, except at the front of the eyewall of Storm IV. Meaning of curves is the same as in Fig 3.5, with the addition of the dashed line in the left panels, which shows the azimuthal-mean flow.

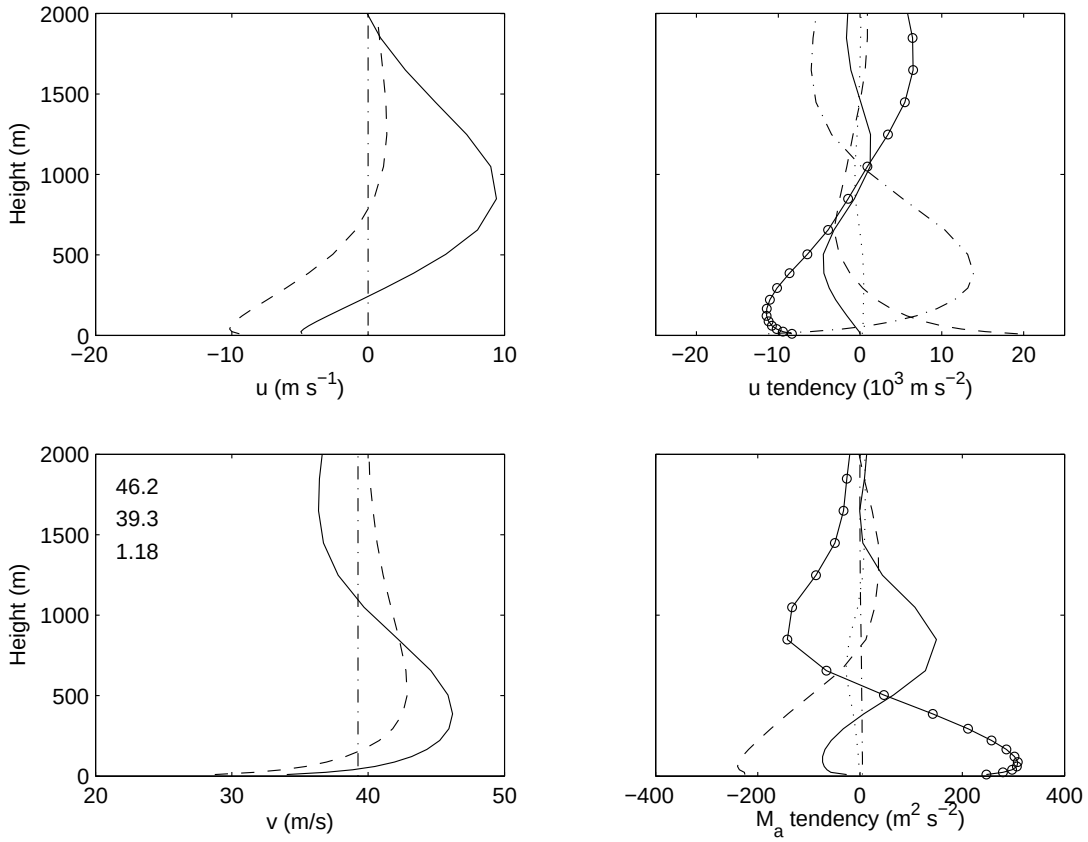

Figure 3.18 The same as Fig 3.17, except at the left of the eyewall of storm IV.

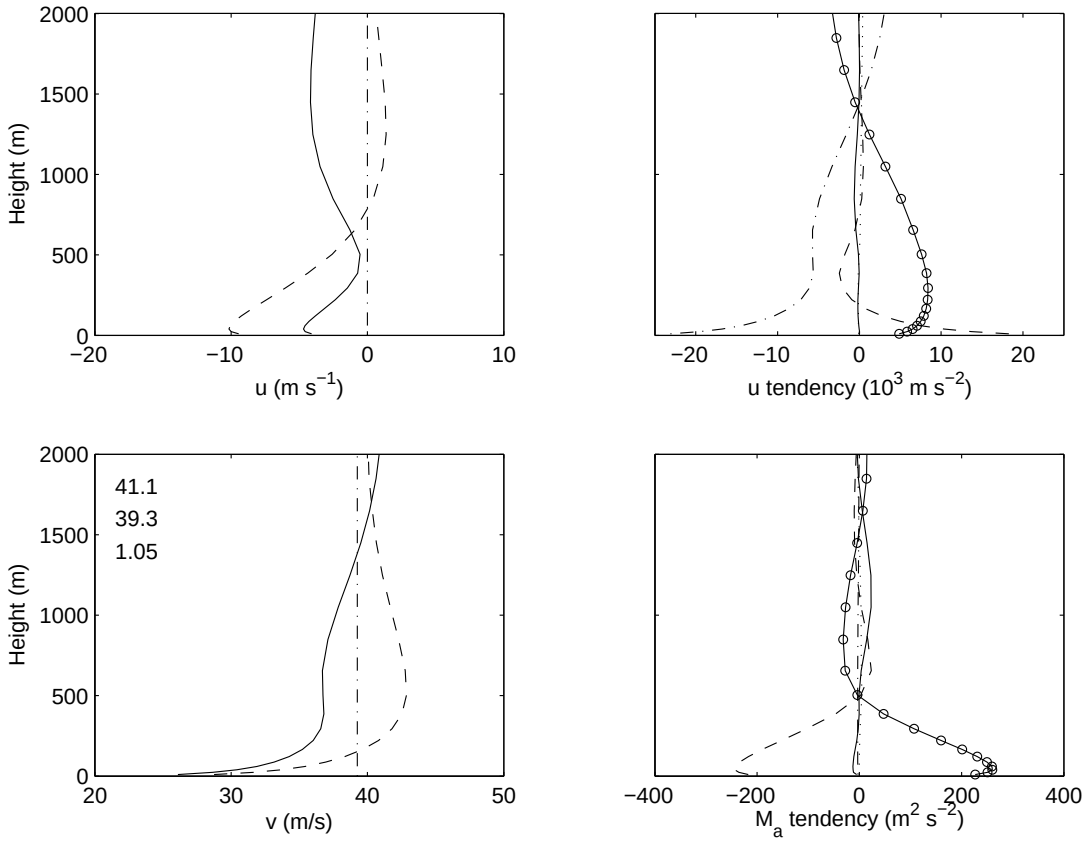

Figure 3.19 The same as Fig 3.17, except at the back of the eyewall of storm IV.

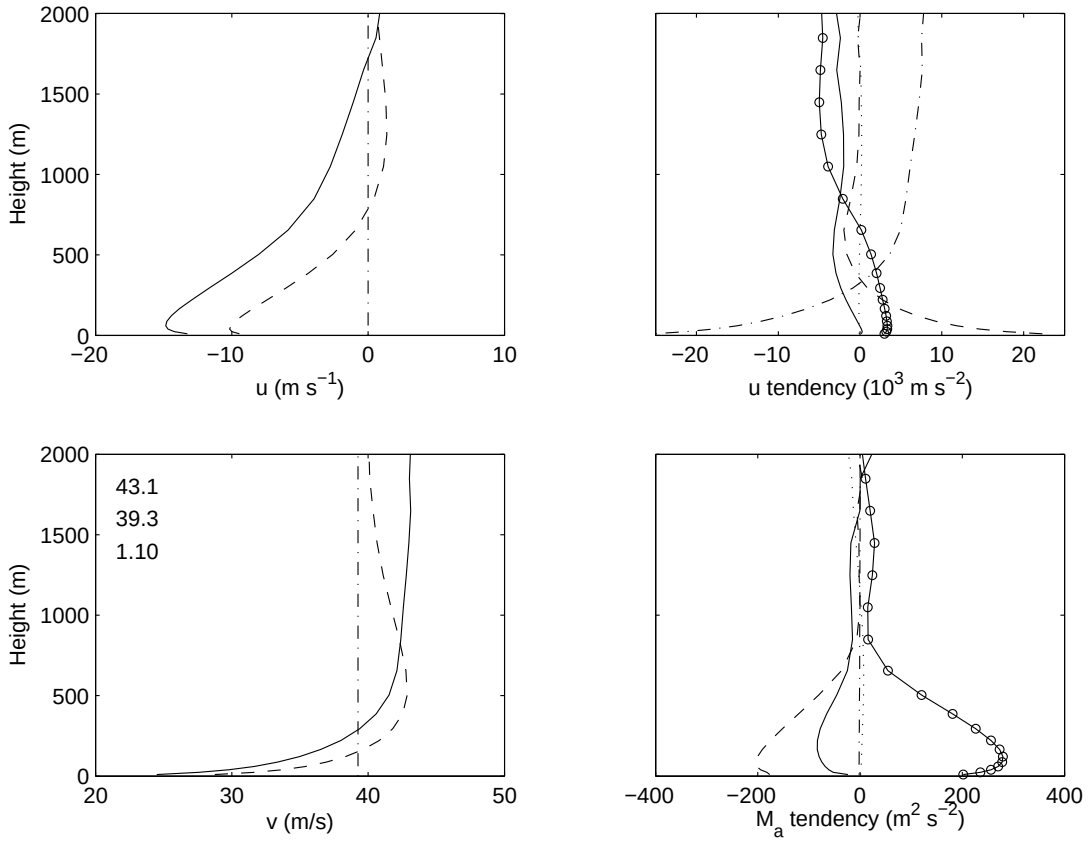

Figure 3.20 The same as Fig 3.17, except at the right of the eyewall of storm IV.

3.5 Summary and Conclusions

In this chapter, a high resolution numerical model, with a sophisticated turbulence closure and surface layer parameterisation, was presented and used to extend the linear analysis of chapter 2 to include the nonlinear terms. It was found in chapter 2 that a supergradient jet could be produced by strong inwards advection of angular momentum, with the inflow maintained against gradient adjustment by upwards diffusion. The main conclusion from this chapter is that including the nonlinear terms and particularly the vertical advection of radial wind provided enhanced inflow forcing and allows a jet that is several times more supergradient than in the linear model, and therefore more realistic. In particular, the wind maxima were found here to be up to approximately 10% to 25% supergradient in a stationary cyclone, with the jet being more supergradient in a more intense system, or near the RMW in a storm with a peaked radial gradient-wind profile.

The linear model did, however, predict a jet height in close agreement with that obtained from the numerical model, especially in the inertially stable case. This seems to be because the height scale set by the turbulent diffusivity and inertial stability, $\delta_0 = (2K/I)^{1/2}$, also defines the height at which the frictionally induced updraft becomes fully established. Thus the introduction of vertical advection to the linear model does not bring any new height scales, but instead is governed by an already existing one.

Is the jet, then, nothing more than the weakly supergradient flow found near the top of the Ekman boundary-layer? In chapter 2, it was argued that the answer is essentially yes; albeit with the complication of three separate components in a moving storm, and several reasons were given for such dynamics being more realistic in the tropical cyclone boundary-layer than elsewhere in the atmosphere. In particular, the linear model used a slip surface boundary condition, buoyant generation of turbulence

would be expected to be minor in a tropical cyclone boundary-layer, and baroclinicity is weak. However, it was shown here that vertical advection plays a crucial role in strengthening the jet, giving a supergradient component several times stronger than in the linear model. The major role of upwards advection may well be peculiar to intense vortices and does not occur in more normally considered cases. This is because the rapid, almost step-like increase in inertial stability near the radius of maximum winds produces an updraft which is much stronger than would be expected from the classical theory, in which the updraft is proportional to the curl of the surface stress. The earlier answer to this question is thus qualified, by adding that nonlinearities – particularly vertical advection – significantly modify the Ekman profiles, giving markedly stronger agradient flow in the upper part of the spiral.

The spatial distribution of the jet in the axisymmetric storm was found to depend upon the "peakiness" of the radial gradient-level wind profile. A compact storm with a relatively rapid decrease in wind speed outside the radius of maximum wind tended to produce a strong jet confined to the immediate vicinity of the eyewall, while a more inertially stable radial profile resulted in a more widely distributed but less intense jet. The difference was explained in terms of the different angular momentum profiles of the two storms, and the consequently differing abilities of the two storms to generate significant horizontal advection of angular momentum.

For a moving storm, it was found that the jet was generally located in the left-forward quadrant of the storm in the Northern Hemisphere, away from the strongest earth-relative near-surface winds in the right-forward quadrant. The asymmetric part of the flow was found to decay more slowly with height than the symmetric, in agreement with the linear results.

Surface-wind reduction factors were calculated and the largest values were found to be near the radius of maximum winds, and to the left of the storm (Northern Hemisphere). Their distribution is thus similar to that of the jet. It was shown that some caution may be necessary in choosing a level for comparison in calculating these, as the asymmetric component can still be large as high as 2 km above the surface in the nonlinear model.

The use of a universal constant for surface-wind reduction is thus shown by both the linear and numerical models to be incorrect. In one sense, this is hardly surprising as the strong contribution of horizontal advection to the momentum budgets means that the assumption of one-dimensionality in profile models is invalid. The variability in the reduction factor between different observational studies is similar to that found here. Powell and Black (1990) have shown that differences in the static stability can explain some of the observed variability in the SWF. These are not present here, and so it is suggested that these dynamical factors are another major reason for the observed variability.